DISSERTATION

# GEOMETRICALLY AND MATERIALLY NONLINEAR ANALYSIS USING MATERIAL POINT METHOD

Submitted by

Abdullah N. Asiri

Department of Civil and Environmental Engineering

In partial fulfillment of the requirements

For the Degree of Doctor of Philosophy

Colorado State University

Fort Collins, Colorado

Summer 2022

Doctoral Committee:

Advisor: Paul Heyliger

John van de Lindt
Suren Chen
Margaret Cheney

# ABSTRACT

## GEOMETRICALLY AND MATERIALLY NONLINEAR ANALYSIS USING MATERIAL POINT METHOD

Computational engineering has become an effective tool for different engineering aspects. It provides suitable simulation models for complex problems. Also, the computational models are strongly recommended as alternatives to experiments due to the consumed cost and time. In addition, because this field has gotten attention earlier, the accuracy of computational models has been improved.

The finite element method (FEM) is one of the famous computer simulations that has been adopted widely in scientific and technical fields. It considers an excellent tool for different engineering analyses; however, for the large deformation behavior, the FEM can not withstand due to the finite discretization of the systems in which the accuracy would be lost as a result of the large distortion that occurred for the model. Thereby, the mesh-less methods are appropriate models for such problems. The material point method (MPM) is one of the improved mesh-less methods, which is an extension of the Particle In Cell (PIC) method used for fluid mechanics modeling.

Both static and dynamic applications are intended to simulate the two-dimensional material point method model. The main objective here is to simulate and validate the material point method with the analytical solutions for different solid mechanics applications. Further, to examine the formulation of the nonlinear behavior using the MPM. The research can be achieved by studying two hypotheses: 1) Beam mechanics analysis using the material point method and 2) Damage mechanics analysis using the material point method. Both hypotheses consider different assumptions of the geometry and material constants. Material point simulation of the two hypotheses will be conducted through RMACC Summit Supercomputer using FORTRAN and MATLAB languages.

ACKNOWLEDGEMENTS

I would like to express my deepest appreciation to my adviser Dr. Paul Heyliger for the support and the advice that the research would not have been possible without him. I'm extremely grateful to Dr. John van de Lindt, Dr. Suren Chen, and Dr. Margaret Cheney for their cooperation and acceptance of being my committee members.

I would like to extend my sincere thanks to my family for their continuous support in my academic life until now. I'm also grateful for my wife, who never let you down.

I cannot leave Colorado State University without mentioning the role of King Khaled University during the whole seven years of my academic studying. Especial thanks for their cooperation and guidance, along with the supportive tool that they provided for many years.

TABLE OF CONTENTS

ABSTRACT ii

ACKNOWLEDGEMENTS iii

LIST OF TABLES vii

LIST OF FIGURES viii

1 INTRODUCTION 1

1.1 Large Deformation Analysis . . . . . . . . . . . . . . . . . . . . . . . . . . 1

1.2 Material Point Method . . . . . . . . . . . . . . . . . . . . . . . . . . . . 3

1.3 Problem Statement . . . . . . . . . . . . . . . . . . . . . . . . . . . . . . 6

2 CONTINUUM MECHANICS CONCEPTS 8

2.1 Motion and deformation . . . . . . . . . . . . . . . . . . . . . . . . . . . 8

2.2 Strain Measures . . . . . . . . . . . . . . . . . . . . . . . . . . . . . . . . 9

2.3 Stress Measures . . . . . . . . . . . . . . . . . . . . . . . . . . . . . . . . 10

2.4 Conservation equations . . . . . . . . . . . . . . . . . . . . . . . . . . . . 11

2.4.1 Conservation of mass . . . . . . . . . . . . . . . . . . . . . . . . . 11

2.4.2 Conservation of linear momentum . . . . . . . . . . . . . . . . . . 12

2.4.3 Conservation of energy . . . . . . . . . . . . . . . . . . . . . . . . 12

2.5 Constitutive equations . . . . . . . . . . . . . . . . . . . . . . . . . . . . 12

2.5.1 Neo-Hookean . . . . . . . . . . . . . . . . . . . . . . . . . . . . . 13

2.6 Strong form . . . . . . . . . . . . . . . . . . . . . . . . . . . . . . . . . . 13

2.7 Weak form . . . . . . . . . . . . . . . . . . . . . . . . . . . . . . . . . . . 15

3 MATERIAL POINT METHOD 19

3.1 Discretization and Material Point Method Algorithms . . . . . . . . . . . 19

3.1.1 Mass Matrix . . . . . . . . . . . . . . . . . . . . . . . . . . . . . . 19

3.1.2 Nodal Velocities Determination . . . . . . . . . . . . . . . . . . . . . . 20
3.2 Material Point Method Algorithms . . . . . . . . . . . . . . . . . . . . . . 21
3.2.1 Standard Formulation (USL) . . . . . . . . . . . . . . . . . . . . . . 21
3.2.2 Modified Updated Stress Last (MUSL) . . . . . . . . . . . . . . . . . 22
3.2.3 Total Lagrangian Material Point method (TLMPM) . . . . . . . . . . 23
3.3 Shape Functions of MPM . . . . . . . . . . . . . . . . . . . . . . . . . . . 26
3.3.1 Shape Functions Properties . . . . . . . . . . . . . . . . . . . . . . . 26
3.3.2 Linear Lagrangian Function . . . . . . . . . . . . . . . . . . . . . . . 28

4 BEAMS MECHANICS ANALYSIS USING THE MATERIAL POINT METHOD 29
4.1 Linear Beams Mechanics Analysis . . . . . . . . . . . . . . . . . . . . . . . 29
4.1.1 Introduction and Literature Review . . . . . . . . . . . . . . . . . . . 29
4.1.2 Static Bar Analysis . . . . . . . . . . . . . . . . . . . . . . . . . . . 32
4.1.3 Dynamic Bar Analysis . . . . . . . . . . . . . . . . . . . . . . . . . . 34
4.1.4 Static Cantilevered Beam Analysis . . . . . . . . . . . . . . . . . . . 39
4.1.5 Static Simply Supported Beam Analysis . . . . . . . . . . . . . . . . 40
4.1.6 Forced vibration of Cantilever Beam . . . . . . . . . . . . . . . . . . 42
4.1.7 Free Vibration of Cantilever Beam . . . . . . . . . . . . . . . . . . . 46
4.1.8 Free Vibration of Simply Supported Beam . . . . . . . . . . . . . . . 48
4.1.9 Free Vibration of Fixed-Fixed Beam . . . . . . . . . . . . . . . . . . 50
4.1.10 Free Vibration of Fixed-Hinged Beam . . . . . . . . . . . . . . . . . 53
4.2 Large Deformation of Beams Mechanics . . . . . . . . . . . . . . . . . . . . 55
4.2.1 Introduction . . . . . . . . . . . . . . . . . . . . . . . . . . . . . . . 55
4.2.2 Nonlinear free vibration of Simply Supported Beam . . . . . . . . . . 55
4.2.3 Nonlinear free vibration of Fixed - Fixed Beam . . . . . . . . . . . . 56
4.2.4 Nonlinear free vibration of Fixed - Hinged Beam . . . . . . . . . . . 59
4.2.5 Total Lagrangian Material Point Method . . . . . . . . . . . . . . . . 59

5 DAMAGE MECHANICS USING MATERIAL POINT METHOD 63

5.1 Damage Constitutive Model . . . . . . . . . . . . . . . . . . . . . . . . . 64

6 AXISYMMETRIC SOLID 68

6.1 Basic Formulation . . . . . . . . . . . . . . . . . . . . . . . . . . . . . . 68

6.1.1 Displacement field . . . . . . . . . . . . . . . . . . . . . . . . . 68

6.1.2 Strain field . . . . . . . . . . . . . . . . . . . . . . . . . . . . . 69

6.1.3 Stress field . . . . . . . . . . . . . . . . . . . . . . . . . . . . . 70

6.1.4 Constitutive equation . . . . . . . . . . . . . . . . . . . . . . . 70

6.2 Trajan's Column . . . . . . . . . . . . . . . . . . . . . . . . . . . . . . 71

6.3 Phyllostachys Edulis bamboo . . . . . . . . . . . . . . . . . . . . . . . 75

7 DISCUSSION AND CONCLUSION 78

7.1 Material points number Influence . . . . . . . . . . . . . . . . . . . . . 78

7.1.1 Material points number impact on displacement response . . . . . . . 78

7.1.2 Material points number impact on frequency response . . . . . . . . . 78

7.2 Time integration of Material Point Method . . . . . . . . . . . . . . . . . 79

7.3 Strain Measures in Material Point Method . . . . . . . . . . . . . . . . . 79

7.4 Euler-Bernoulli beam behavior . . . . . . . . . . . . . . . . . . . . . . . 80

7.5 Element Size Effect . . . . . . . . . . . . . . . . . . . . . . . . . . . . . 82

7.6 Conclusion . . . . . . . . . . . . . . . . . . . . . . . . . . . . . . . . . . 84

References 86

LIST OF TABLES


1 The relations between stress measures . . . . . . . . . . . . . . . . . . . . . . 11

2 Bar axial displacements and strains, $\nu = 0.0$ . . . . . . . . . . . . . . . . . . . . . 34

3 Bar axial displacements and strains, $\nu = 0.3$ . . . . . . . . . . . . . . . . . . . . . 35

4 Transverse deflection of the end of cantilever beam . . . . . . . . . . . . . . . . 39

5 Transverse deflection at the middle of simply supported beam . . . . . . . . . . 42

6 First three natural frequency of cantilever beam . . . . . . . . . . . . . . . . . . 48

7 First three natural frequency of simply supported beam . . . . . . . . . . . . . . 50

8 First three natural frequency of fixed-fixed beam . . . . . . . . . . . . . . . . . 52

9 First three natural frequency of fixed-hinged beam . . . . . . . . . . . . . . . . 53

10 $(\omega_{NL}/\omega_L)^2$ ratio for simply supported beam . . . . . . . . . . . . . . . . . . . 56

11 $(\omega_{NL}/\omega_L)^2$ ratio for Fixed-Fixed beam . . . . . . . . . . . . . . . . . . . . . 59

12 $(\omega_{NL}/\omega_L)^2$ ratio for Fixed-Hinged beam . . . . . . . . . . . . . . . . . . . . 61

13 Mechanical properties of the Phyllostachys edulis bamboo . . . . . . . . . . . . 76

14 Frequency values for different strain measures . . . . . . . . . . . . . . . . . . . . 80

LIST OF FIGURES


1 The Lagrangian description (top) and Eulerian grid (bottom) . . . . . . . . . . . 4

2 Material point method general computational steps . . . . . . . . . . . . . . . . . . 5

3 Difference betweem ULMPM and TLMPM (Retrieved from [10]) . . . . . . . . . . 25

4 The bar geometry . . . . . . . . . . . . . . . . . . . . . . . . . . . . . . . . . . . . 33

5 Axial displacement of cantilevered bar . . . . . . . . . . . . . . . . . . . . . . . . 37

6 Particle velocity of cantilevered bar . . . . . . . . . . . . . . . . . . . . . . . . . 38

7 Geometrical description of the cantilevered beam . . . . . . . . . . . . . . . . . . 40

8 Initial MPM mesh of cantilever beam . . . . . . . . . . . . . . . . . . . . . . . . 40

9 Cantilevered beam deflection compared with analytical solution . . . . . . . . . 41

10 MPM mesh of simply supported beam with 64 points . . . . . . . . . . . . . . . 42

11 Vertical deflection of simply supported beam . . . . . . . . . . . . . . . . . . . . 43

12 First three natural frequencies of vibration of cantilever beam . . . . . . . . . . 45

13 MPM normal modes compared to beam theory analysis . . . . . . . . . . . . . . 47

14 MPM normal modes compared to beam theory analysis . . . . . . . . . . . . . . 49

15 MPM normal modes compared to beam theory analysis . . . . . . . . . . . . . . 51

16 First mode shape at different time steps . . . . . . . . . . . . . . . . . . . . . . 52

17 MPM normal modes compared to beam theory analysis . . . . . . . . . . . . . . 54

18 Nonlinear frequencies for simply supported beam when $L/r = 27.713$ . . . . . . 57

19 Nonlinear frequencies for Fixed-Fixed beam when $L/r = 27.713$ . . . . . . . . . 58

20 Nonlinear frequencies for Fixed- Hinged beam when $L/r = 27.713$ . . . . . . . . 60

21 Vertical bar vibration under gravity load . . . . . . . . . . . . . . . . . . . . . . 62

22 Free vibration of bar using TLMPM . . . . . . . . . . . . . . . . . . . . . . . . 62

23 Cantilever beam results (red dashed line) compared to Heyliger and Reddy results [22] . . . . . . . . . . . . . . . . . . . . . . . . . . . . . . . . . . . . . . . . 63

24 Axisymmetric solid . . . . . . . . . . . . . . . . . . . . . . . . . . . . . . . . . . 68

25 Some axisymmetric structures . . . . . . . . . . . . . . . . . . . . . . . . . . . . 69

26 Stresses acting on a differential volume of an axisymmetric solid underaxisymmetric loading . . . . . 70
27 Trajan's column . . . . . 72
28 Trajan's cloumn drums distrubution . . . . . 72
29 Typical marble stress-strain curve by Anastasiadis et al [2] . . . . . 73
30 Stress- strain curve of Trajan's column (Red dashed lines) compared with laboratory test of Carrara marble of Mahmutoglu [34] . . . . . 74
31 Phyllostachys Edulis bamboo . . . . . 75
32 MPM mesh of Phyllostachys Edulis bamboo . . . . . 76
33 MPM Compression test result (Red dashed lines) compared to experimental result of Phyllostachys edulis bamboo by Li et al. [30] . . . . . 77
34 First mode shape of simply supported beam . . . . . 81
35 Deformed cross section of beam L = 8 at $\frac{L}{4}$ . . . . . 82
36 First mode shape of simply supported beam . . . . . 83
37 Deformed cross section of beam L = 16 at $\frac{L}{4}$ . . . . . 84
38 Element size effect of material point method . . . . . 85

# 1 INTRODUCTION

## 1.1 Large Deformation Analysis

Flexible structures were used widely in the solid mechanics field. For example, suspension systems in automobiles use the leaf springs components. Helical springs are used for absorbing the shock of the motorcycles. Transmission cables could experience large deflection. All of these lead to model of advanced computational methods to evaluate the structure's capacity and predict and understand the behavior of such flexible structures. In modeling flexible structure, dealing with rigid body motion is a crucial issue because the rigid body motions have no strain. Thus, the strain measures need to neglect the impact of the rigid body rotations. Therefore, Green-Lagrange strains are used widely in large deformation analysis. Also, different procedures have been proposed a Lagrangian formulation with corotated references. While Pai and Nayfeh [47, 46] used the local displacements and local reference configuration to obtain objective strains (strains without rigid body rotations) also, they used the local engineering stresses and strains to introduce the derivation of the geometrically-exact structural theories.

In large deformation analysis of structures, the Lagrangian formulation is widely adopted because the structure has a standard configuration that the body would experience after the load removes. Further, the incremental procedure is used for solving the Lagrangian formulations because the stiffness of the structure is a function of the displacements[45].

A Total Lagrangian approach of the two-dimensional curved beam was made by Surana [60]. The displacement is assumed by using two translations DOFs for the node and a rotational DOF about the axes normal to the plane. A fully nonlinear strain-displacement relation has been studied by Pai et al. [45] for flexible beams. The authors used Jaumann stress and strain measures. The results of the finite element model were verified using two fixtures experiments data. A satisfactory agreement for the numerical results with experimental data has been obtained. Later, Nankorn [39] provided a total Lagrangian formulation of a two-dimensional Euler-Bernoulli beam using field-consistent interpolations. The interpolations are expressed in terms of polynomials for both transverse and axial displacements. A rotational vector of the new Riessner's beam element has been introduced by Makinen [35] based on the total Lagrangian description. Post-buckling analyses of laminated composite beams were examined by Pagani and Carrera [43] using Carrera Unified formulation while the governing equations were derived using the total Lagrangian approach. Recently, nonlinear free vibration of anisotropic beams using total Lagrangian elasticity formulation has been introduced by Heyliger and Asiri [20]. A fully nonlinear strain was adopted in the analysis. The results are compared with the finite element model of the Euler-Bernoulli beam using Föppl–von Karman nonlinearity.

Several aspects of the large deformation of beams have been done. Reissner [50] studied the plane behavior of beams due to large deformation by introducing new constitutive relations including the axial strain, shear strain, and bending strain. At the same time, the equilibrium equations were solved using the virtual work concept. While Irschik and Gerstmaryr [25] extended this concept for the Euler-Bernoulli model of the beam by eliminating the shear force influence. Also, Humer and Irschik [23] included sliding boundary conditions with a continuum-based derivation.

Abedinnasab et al. [1] derived the nonlinear governing equation using Hamilton principal for the Euler-Bernoulli beams. The authors used Green-Lagrange strains tensor as the strain formulation of the large deformation. Modified couple stress theory was used by Park and Gao [48] for the Euler-Bernoulli beam. The introduced model has been included the size effect by tracking the internal material length. A new matrix displacement approach has been developed by Yang [64]. The large displacement is considered with the midpoint tangent incremental method to study the large deformation of the cantilever beam. One of the published studies of the elastic theory of beam is developed by Steigmann [56] where three-dimensional rods are considered. The Kirchhoff-Clebsch theories are used to model the flexural response.

The finite difference method and finite element method are usually used for analyzing the large deformation of the elastic structure. For instant, the finite difference method was used to analyze the fully nonlinear beam equations that were subjected to large static displacement by Minguet and Dugundj[38]. Finite element method is commonly method that adopted in nonlinear analysis (e.g. Bathe[5]; Bauchau and Hong [6]; Heyliger and Reddy [22]). However, the finite element method produces a large distortion in the case of the large deformation analysis because of the existence of the mesh. Therefore, mesh-less methods have taken place in studying structure behaviors that undergo large deformation. Starting with a particle in cell method through smoothed particle Hydrodynamic concept through until the material point method that introduced by Sulsky and Schreyer [58]. The next section discusses the history of the material point method used in this research.

## 1.2 Material Point Method

Different mesh-less frameworks have been developed. Starting with the earlier MMs that were introduced by Gingold and Monaghan[18]and Lucy [32] which called Smoothed Particle Hydrodynamic (SPH) was concerned about the modeling of astrophysical events. Later, a finite difference method was developed by Liszka and Orkisz [31]; then, the diffuse element method (DEM) by Nayroles, Touzot, and Villon [40]. Then, the material point method by Sulsky et al.[57] which is adopted in this research.

The material point method is one of the improved mesh-less methods. It has considered an extension of the particle in cell method introduced by Harlow[19] for fluid mechanics modeling. However, PIC suffers from an energy dissipation issue, which impacts the method's accuracy. Later, The Fluid implicit Particle method (FLIP) took place by Brackbill and Ruppel [26]. FLIP was first used for fluid simulation. Later, Sulsky et al.[57, 59] provided a modification of this method to be implemented for solid mechanics formulation. As a result, the material point method has been named for this modification by Sulsky and Schreyer[58].

MPM concept depends on two field descriptions; Lagrangian description and Eulerian grid, as described in Figure 1. A continuum body in the material point method is discrete into multiple numbers of particles (points). These particles are defined as Lagrangian material particles. The Lagrangian description of particles means that the particles are embedded and deformed with the material. Each particle has a position, mass, density, volume, deformation gradient, and Cauchy stress tensor. The particle's mass keeps constant through the process while the volume changes due to the deformation of the material. These particles are tracked in the deformation process. The background grid of the continuum body allows the body to deform in the same grid that describes the updated Lagrangian scheme introduced by Sulsky where also the equation of momentum is solved. However, in the Total Lagrangian material point method (TLMPM) that has been done by de Vaucorbeli et al.[9], the continuum body occupies the background grids only in the reference configuration. To better understand the continuum of solid concepts, one can refer to the chapter two for further discussion.

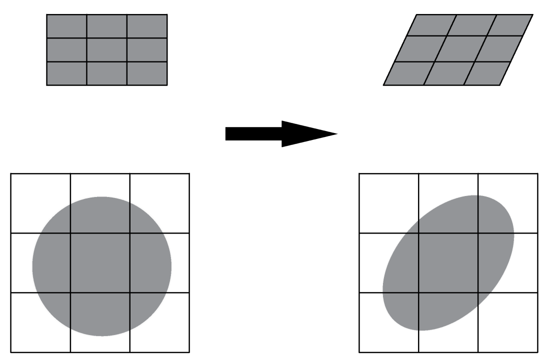

Figure 1: The Lagrangian description (top) and Eulerian grid (bottom)

The material point method (MPM) algorithm was existed initially to analyze some straightforward problems in solid mechanics [57]. Thereby, different material point method algorithms have been developed to solve such problems explicitly, giving more efficient procedures than implicit solutions. The explicit solutions are considered the simplest form, following the updated Lagrangian MPM approach. However, the total Lagrangian material point method (TLMPM) can be developed from the updated Lagrangian MPM with the same simple modification. Figure 2 shows the MPM general algorithm where the first step is transferring (mapping) the particle information to the grid. Next, the balance equation of momentum is solved on the nodes. Then, all the particles' information and variables positions, volume, density, stresses, etc are updated from the node to the particles. In the end, the grid reconstructs to the initial status. This final reconstruction prevents distortion from occurring, allowing the material point method to be a suitable approach for large deformation problems.

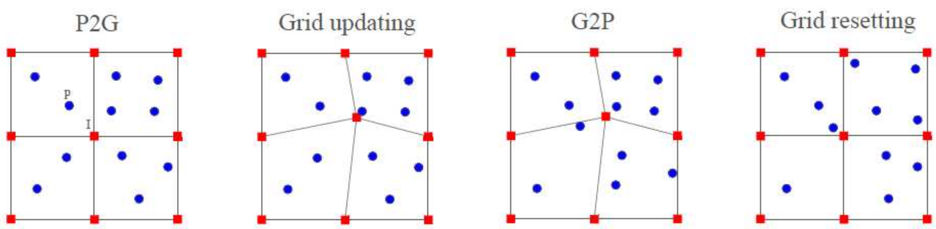


Figure 2: Material point method general computational steps

Since the introduction of the MPM, few algorithms have been developed; the updated stress last (USL) is the standard material point algorithm developed by Sulsky et al.[57]. However, this technique generates a numerical issue corresponding to the small particle mass. Thus, Sulsky et al.[59]extended the formulation to the modified updated stress last (MUSL), where the updated particles' velocity mapped back to the nodes to avoid the small mass issue. Further, the Total Lagrangian MPM formulation was developed by de Vaucorbeli et al.[9] to track the nonlinear behavior under large load impact.

The MPM has some advantages that make it an excellent approach to model for such problems. The absence of mesh is considered one of the advantages since the particles carry the analyzed information. Also, the Eulerian grid allows direct and efficient treatment of frictional contacts of multi-bodies because the Eulerian grids cover the entire deformable domain. While MPM performs an easy computer implementation compared to other meshless methods, it also gives good images and simulations. The influence of the comprehensive finite element method studies supports the material point method to be considered due to the similarity of the FEM and MPM.

## 1.3 Problem Statement

The material point method is characteristic in handling large deformation problems of solid continuum mechanics due to the particle-based formulation. However, the static response of solid applications was not a target for many literary works of MPM. The reason behind that is the ability of MPM to represent and visualize multiple interaction problems. Thus, the geotechnical and fluid engineering fields are the most leaded fields that got the characteristics of the MPM. Recently, as de Vaucorbeli et al. [10] stated, "We observe a lack of MPM formulations for structural elements such as beams and shells." Therefore, the static response of linear behavior of bars is introduced and validated along with the analytical solution based on the linear elasticity formulation. The aim is to study the particle behaviors under the different assumptions of the geometry and material constants like modulus of elasticity and the Passion's ratio. Based on the best knowledge, a dynamic analysis of the linear bar problem has gotten little attention in the literature due to the time-dependent formulation that MPM provides. The validation with the analytical solution also takes place to examine the accuracy of the material point formulation.

Further, different effects of loads assumption and the variety of the examined geometry must get more attention in MPM. These play roles in the convergence study of the MPM with other formulations as well as enrich the solid mechanic's literature of this new approach. The static linear behavior of the beams is studied in this research. The MPM results compared with the analytical solutions introduced by Timoshenko and Goodier[61] where the material constants impact the response as well as the assumed boundary conditions for linear beam displacements. Since the domain of the studied structure is represented with a set of material particles, this allows the examiners to track the behavior of the structure effectively in any desired location and time. Further, How the material points numbers would play a role in convergence with the analytical solution. These would increase the consideration of the MPM of such problems and provide a suitable introduction for examining the nonlinear behavior problems.

Unlike grid-based methods such as the finite element method, creating an efficient and accurate model of the nonlinear behavior using the material point method is reasonable due to the absence of the mesh that provides a solution for the structure under large loads. The model could handle any Eulerian grid dimensions embedded with material particles and the impact of the different material constants in the nonlinear behavior. Therfore, the geometrically nonlinear free vibration of beams has been studied for different geometrical assumptions.

In the solid mechanics field, the total Lagrangian MPM was introduced by de Vaucorbeil et al.[9]. A total Lagrangian MPM (TLMPM) is established using the FORTRAN language to examine the very large deformations of solids. In TLMPM, the stress and strains are defined in the reference configuration where the nonlinear constitutive equations are employed to track the large deformation of the solid. At the same time, the spatial derivatives are computed concerning the material coordinates. TLMPM is considered an efficient formulation due to the resistance that TLMPM provides in cell-crossing error and numerical fracture. The weak forms in this formulation is represented by the integrals referred to the reference configuration. The procedures of TLMPM are almost identical to the standard MPM. The objective is to study the structure behavior using this new TLMPM with various load and geometry assumptions[10]. Algorithms 1 represents the stranded MPM procedure that will be adopted in this research.

# 2 CONTINUUM MECHANICS CONCEPTS

## 2.1 Motion and deformation

Consider body in undeformed configuration;this configuration can be defined as $\boldsymbol{X}$ which is considered as Lagrangian coordinate. This body can be formed by multiple material points that include specific material properties. If the body moves to the deformed configuration, the same material points are now described by $\boldsymbol{x}$ which refers to the Eulerian coordinate or spatial coordinate. The solid deformation "motion" is expressed by $\phi(X, t)$ . Thus, the relationship between the reference " undeformed" configuration coordinates and current "deformed" configuration coordinates is given as follows

$$x = \phi(X, t) \tag{2.1}$$

From this, the relationship between displacement, velocity and acceleration is established. The displacement of the material points can be described as the difference between the current location and the reference location with consideration of the initial time that corespondents to the reference configuration $t = 0$. The displacement can be expressed as

$$u(X, t) = \phi(X, t) - \phi(X, 0) = x - X \tag{2.2}$$

while the velocity of the material point $X$ is described as the rate of change in the location of the corespondents material point as

$$v(X, t) = \frac{\partial \phi(X, t)}{\partial t} \tag{2.3}$$

and the acceleration is defined as the rate of change in velocity of the corespondents material point, which expressed as

$$a(X, t) = \frac{\partial v(X, t)}{\partial t} \tag{2.4}$$

The deformation gradient tensor is another concept that introduces the mapping function that maps every linear element $dX$ in the reference configuration to the current configuration after the deformation occurred. The expression of the deformation gradient is as follows

$$F = \frac{\partial \phi}{\partial X} = \frac{\partial \ x}{\partial X} \tag{2.5}$$

**Material Time Derivative**

Consider the field of a body that is defined as $\boldsymbol{\phi}$ this field might be scalar, vectorial, or tonsorial. The field should be tracked to determine the rate of change for a given material point $\mathbf{X}$. This concept is called the material time derivatives of $\boldsymbol{\phi}$. This description has two different definitions according to the variables adopted in desired the application:

1. The Lagrangian description: Lagrangian description considers the material coordinates $\mathbf{X}$ and time $t$ are independent variables. The material time derivative is computed by taking the partial derivatives of the field with respect to time. The material field can be expressed as

$$\frac{D\phi(X,t)}{Dt} = \frac{\partial \phi(X,t)}{\partial t} \tag{2.6}$$

Because the MPM considers the Lagrangian description, the material time derivative is applicable straightforward.

2. Eulerian description: In the Eulerian description, the material time derivative is not easy to determine since the change occurred to the spatial coordinate $x$ along with time $t$. This requires applying the derivatives in terms of material description with consideration of the material coordinate $\mathbf{X}$.

## 2.2 Strain Measures

To map the body elements from undeformed states and deformed states, we need to consider the strain measures. In continuum mechanics, the strain measures are different depending on the deformation behavior. If a large deformation takes place, the nonlinear strain measures should be applied. Here is a review of the nonlinear strain measures which are widely adopted in large deformation modeling like the Green strain tensor, the rate of deformation tensor, and the right Cauchy-Green strain tensor.

The right Cauchy-Green deformation tensor is given as

$$C = F^T.F \tag{2.7}$$

where the $F^T$ is the transpose operator of the deformation gradient. While the Green strain tensor is the difference between the squared element length $dx$ and $dX$ written as

$$E = 1/2(F^T.F - I) = 1/2(C - I) \tag{2.8}$$

The velocity gradient tensor is written as

$$L = \frac{\partial v}{\partial x} \tag{2.9}$$

which supports the material time derivatives of the deformation gradient to expressed as The rate of deformation tensor **D** is defined as

$$D = 1/2(L + L^T), W = 1/2(L - L^T) \tag{2.10}$$

where D describes the rate of stretching and shearing.

## 2.3 Stress Measures

The stress measures work unite with the strain measures [9]. The most stress tensors measures are; 1) Cauchy stress, 2)Kirchhoff stress, 3) First Piola-Kirchhoff stress ($1^{st}$ PK) and 4) Second Piola-Kirchhoff stress ($2^{nd}$ PK). The Cauchy stress is the real stress that is consid-

Table 1: The relations between stress measures

| | Cauchy stress $\sigma$ | Kirchhoff stress $\tau$ | $1^{st}$PK P | $2^{nd}$PK S |
|---|---|---|---|---|
| $\sigma$ | — | $\tau J^{-1}$ | $J^{-1}PF^T$ | $J^{-1}FSF^T$ |
| $\tau$ | $J\sigma$ | — | $PF^T$ | $FSF^T$ |
| P | $J\sigma F^{-T}$ | $\sigma J^{-1}$ | — | FS |
| S | $JF^{-1}\sigma F^{-T}$ | $F^{-1}\tau F^{-T}$ | $F^{-1}P$ | — |

ered along with the rate of deformation **D** with respect to deformed volume. The Kirchhoff stress is weighted Cauchy stress that works unite with the deformation rate with respect to the undeformed volume. At the same time, the $1^{st}$ Piola-Kirchoff stress takes place along with the deformation gradient, where both appear at the explicit MPM formulation. Also, it is considered an unsymmetric stress tensor. The $2^{nd}$ Piola-Kirchoff stress tensor works with the Green strain tensor, which is a material symmetric stress tensor. To explain the relations of the stress measures, Table 1 provides a brief explanation.

## 2.4 Conservation equations

There are four different conservation laws in continuum mechanics [10]. These laws can be categorized as; 1) Conservation of mass, 2) Conservation of linear momentum, 3) Conservation of angular momentum and 4) Conservation of energy.

### 2.4.1 Conservation of mass

Generally, the conservation of mass concepts refers to the constant value of body mass under any circumstance that the body can face. The equation of mass conservation can be stated as

$$\frac{D\rho}{Dt} + \rho.\nabla.v \tag{2.11}$$

for the Lagrangian description, the mass conservation equation become

$$\rho.\mathbf{J} = \rho_0 \tag{2.12}$$

### 2.4.2 Conservation of linear momentum

Momenta is defined as the mass of the body multiplied by its velocity. This generalized quantity is equivalent to the required force needed to stop the body at a time unit length (where the Newton 3rd law of motion must be satisfied). The required law to compute the change of linear momentum is equal to the sum of external forces applied to the body that is given by

$$\rho.\frac{D\mathbf{v}}{Dt} = \nabla.\sigma + \rho\mathbf{b} \tag{2.13}$$

### 2.4.3 Conservation of energy

The law states that the rate of change in the total energy in the body must equal the rate of work done by applied forces added to the rate of work heat flux $\mathbf{x}$ and the source of energy (change). This law can be written as

$$\rho.\frac{De}{Dt} = D : \sigma - \nabla.q + \rho s \tag{2.14}$$

where $e$ is the specific internal energy and $\rho s$ donates the source per unit volume.

## 2.5 Constitutive equations

The constitutive relations can apply the expression of the relations between the kinetic quantities and kinematics quantities. From these equations, The examiners can differentiate between solids and fluids, steel and plastic. Robert Hooke developed the more straightforward constitutive equation called *Hooke's law* that used to model the linear elastic materials. For linear elastic isotropic material, the stress tensor can be computed by

$$\sigma_{ij} = \lambda\epsilon_{kk}\delta_{ij} + 2\mu\epsilon_{ij} \tag{2.15}$$

where $\lambda$ and $\mu$ represent Lame' constant. Hence, in MPM, the particle's stress tensor would be updated as following

$$\sigma_p^{t+\Delta t} = \sigma_p^t + (\lambda tr \Delta\epsilon_p)\mathbf{I} + 2\mu\Delta\epsilon_p, \qquad \Delta\epsilon_p = \frac{1}{2}(L_p^{t+\Delta t} + (L_p^{t+\Delta t})^T) \tag{2.16}$$

### 2.5.1 Neo-Hookean

The Neo-Hookean constitutive law is used in modeling the isotropic hyperelastic material where the material parameters in linear elastic conditions are familiar to the Neo-Hookean model. First Piola-Kirchhoff stress $P$ is expressed as a function of deformation gradient matrix $\mathbf{F}$ as follows

$$P = \mu(\mathbf{F} - \mathbf{F}^{-T}) + \lambda lnJ\mathbf{F}^{-T} \tag{2.17}$$

where $J$ is the determinaint of deformation gradiant $\mathbf{F}$. This stress measure can be convenient to Total Lagrangian formulation.

## 2.6 Strong form

In the updated Lagrangian description, the differential equations of the conservation equations, Kinematics equations and boundary conditions can be expressed as a whole as

Conservation of mass:

$$\frac{D\rho}{Dt} + \rho.\nabla.v \tag{2.18.A}$$

Conservation of linear momentum:

$$\rho.\frac{D\mathbf{v}}{Dt} = \nabla.\sigma + \rho\mathbf{b} \tag{2.18.B}$$

Conservation of energy:

$$\rho.\frac{De}{Dt} = D : \sigma - \nabla.q + \rho s \tag{2.18.C}$$

Strain measure:

$$\mathbf{D} = sym(\nabla\mathbf{v}) \tag{2.18.D}$$

Constitutive equation:

$$\sigma^{\nabla} = S_t^{\sigma D}(\mathbf{D}, \sigma) \tag{2.18.E}$$

Initial condition:

$$\mathbf{v}(x, t = 0) = \mathbf{v}_0, \sigma(x, t = 0) = \sigma_0 \tag{2.18.F}$$

Essential boundary condition:

$$\mathbf{u} = \bar{u} \text{ on } \Gamma_u \tag{2.18.G}$$

Natural boundary condition:

$$\mathbf{t} = \bar{t} \text{ on } \Gamma_t \tag{2.18.H}$$

where $\rho(X,t)$, $v(X,t)$, and $\sigma(X,t)$ are the density, velocity, and the Cauchy stress tensor, respectively. While the body force represented by $\mathbf{b}$ and $\nabla$ is the gradient corresponding to the deformed configuration. Whereas the $\sigma^{\nabla}$ is representing stress rates related to the large rotations.

Due to the adopted Lagrangian description in MPM, the conservation of mass equation will not be solved in this form. While the values like $\bar{u}$ , $\bar{t}$ , $v_0$ and $\sigma_0$ are considered known values. The independent variables in Lagrangian formulation are the material coordinates $\boldsymbol{X}$ and time $\boldsymbol{t}$. The dependent variables are mass density, velocity $\boldsymbol{v}$ and stress with its 9 components that turns to 6 independent components in isotropic materials. At the same time, there are 17 equations with consideration of the conservation of energy equation. However, because non-isothermal models are not considered in this research, the conservation of energy equation is not PDE and, thus, is not applicable in the model, which turns to 16 equations with 16 unknowns.

## 2.7 Weak form

The weak form of the momentum equation (2.18.B) is expressed as

$$\int_{\Omega} \rho \delta u_i a_i d\Omega + \int_{\Omega} \rho \frac{\partial \delta u_i}{\partial x_j} \sigma^s_{ij} d\Omega = \int_{\Omega} \rho \delta u_i b_i d\Omega + \int_{\Gamma_t} \rho \delta u_i \bar{t}^s_i d\Gamma_t \tag{2.19}$$

This equation represents the last form of the derivation of the momentum equation. Where $\mathbf{\Omega}$ is the current configuration, $\delta u$ is the virtual displacement field, $\sigma^s_{ij}$ is the Cauchy stress and the i,j = 1,2,3. , $a_i$ is the acceleration field while $\bar{t}^s_i$ represents the specific traction vector.

The entire domain $\Omega$ is discretized by a set of material sub-domains $\Omega_p$ in which the total mass of the sub-domain is assumed to be in the corresponding material point; thus, the mass density function can be written as

$$\rho(\mathbf{x}, t) = \sum_{p=1}^{n_p} m_p \delta(\mathbf{x} - \mathbf{x}_p) \tag{2.20}$$

which $\delta$ represents Dirac delta function, $m_p$ is the mass of particle $p$. By applying equation (2.20) into (2.19) that gives

$$\begin{aligned} \rho(\mathbf{x}, t) = \sum_{p=1}^{n_p} m_p \delta u_i(\mathbf{x}_p) a_i(\mathbf{x}_p) + \sum_{p=1}^{n_p} m_p \left. \frac{\partial \delta u_i}{\partial x_j} \right|_{(\mathbf{x}_p)} \\ \sigma^s_{ij}(\mathbf{x}_p) = \sum_{p=1}^{n_p} m_p \delta u_i(\mathbf{x}_p) b_i(\mathbf{x}_p) + \sum_{p=1}^{n_p} m_p \delta u_i(\mathbf{x}_p) \bar{t}^s_i(\mathbf{x}_p) h^{-1} \end{aligned} \tag{2.21}$$

The boundary layer thickness must be introduced when the volume of each particle is identified. The domain is discretized by a finite element mesh. Every cell has nodes $n_n$ with shape function $\phi_I$ corresponding for every node $I$. $x_{iI}$ represents the $i$ component of the position vector of node $I$. The shape functions and derivatives evaluation is identical to the efficient finite element analysis, which does not include neighbor search as other mesh-free methods. So, the position of a node is written as approximated in FE as

$$x_i(\mathbf{x},t) = \sum_{I=1}^{n_n} \phi_I(\mathbf{X}) x_{iI}(t) \tag{2.22}$$

Similar to the Lagrangian finite element, the shape function refers to the undeformed Lagrangian coordinates $\boldsymbol{X}$. Apply the initial configuration when $t = 0$ in equation (2.22) this provides

$$X_i(\mathbf{x},t) = \sum_{I=1}^{n_n} \phi_I(\mathbf{X}) X_{iI} \tag{2.23}$$

where $\mathbf{X}_I$ is the coordinates position of the node $I$ in the initial configuration and the $X_{iI}$ is the component corresponding to $\mathbf{X}_I$. Thus, the displacement can be expressed as

$$u_i = x_i - X_i = \sum_{I=1}^{n_n} \phi_I(\mathbf{X})(x_{iI} - X_{iI}) = \sum_{I=1}^{n_n} \phi_I(\mathbf{X}) u_{iI}(t) \tag{2.24}$$

The velocity and the acceleration fields are written as

$$v_i(\mathbf{X},t) = \sum_{I=1}^{n_n} \phi_I(\mathbf{X}) v_{iI}(t) \tag{2.25}$$

$$a_i(\mathbf{X},t) = \sum_{I=1}^{n_n} \phi_I(\mathbf{X}) a_{iI}(t) \tag{2.26}$$

where the $v_{iI}$ and $a_{iI}$ are the components of the corresponding node $I$ for velocity and acceleration, respectively. Equation (2.25) is going to be used to determine the velocity gradient and update the particle position. Also, equation (2.24) can be approximated by using the shape function as

$$\delta u_i = \sum_{I=1}^{n_n} \phi_I(\mathbf{X}) \delta u_{iI} \tag{2.27}$$

From this, the generated spatial derivatives of $\delta u_i$ is expressed as

$$\frac{\partial \delta u_i}{\partial x_j} = \sum_{I=1}^{n_n} \frac{\partial \phi_I}{\partial x_j} \delta u_{iI} \tag{2.28}$$

Now, apply the finite element approximation " Equations (2.26) to (2.28)" into Equation (2.21) that gives

$$\sum_{p=1}^{n_p} m_p \left[ \sum_{I=1}^{n_n} \phi_I(\mathbf{x}_p) \delta u_{iI} \right] \left[ \sum_{I=1}^{n_n} \phi_J(\mathbf{x}_p) a_{iJ} \right] + \sum_{p=1}^{n_p} m_p \left[ \sum_{I=1}^{n_n} \left. \frac{\partial \phi_I}{\partial x_j} \right|_{(\mathbf{x}_p)} \delta u_{iI} \right] \sigma^s_{ij}(\mathbf{x}_p) = \sum_{p=1}^{n_p} m_p \left[ \sum_{I=1}^{n_n} \phi_I(\mathbf{x}_p) \delta u_{iI} \right] b_i(\mathbf{x}_p) + \sum_{p=1}^{n_p} m_p \left[ \sum_{I=1}^{n_n} \phi_I(\mathbf{x}_p) \delta u_{iI} \right] \bar{t}^s_i(\mathbf{x}_p) h^{-1} \quad (2.29)$$

It is known that the virtual displacement is arbitrary " it can be any possible value", therefor, the Equation (2.29) can be written as

$$\sum_{p=1}^{n_p} m_p \phi_I(\mathbf{x}_p) \left( \sum_{I=1}^{n_n} \phi_J(\mathbf{x}_p) a_{iJ} \right) + \sum_{p=1}^{n_p} m_p \left. \frac{\partial \phi_I}{\partial x_j} \right|_{(\mathbf{x}_p)} \sigma^s_{ij}(\mathbf{x}_p) = \sum_{p=1}^{n_p} m_p \phi_I(\mathbf{x}_p) b_i(\mathbf{x}_p) + \sum_{p=1}^{n_p} m_p \phi_I(\mathbf{x}_p) \bar{t}^s_i(\mathbf{x}_p) h^{-1} \quad (2.30)$$

Equation(2.30) can be expressed in terms of mass matrix, external and internal force vectors as

$$m_{IJ} a_J = f_I^{ext} + f_I^{int}, \qquad I = 1, 2, ..., n_n \quad (2.31)$$

This equation represents the *semi-discrete equation* in which just domain was discretized that is identical to FEM.

The $I\ J$ component of the consistent mass matrix is expressed as

$$m_{IJ} = \sum_{p=1}^{n_p} m_p \phi_I(\mathbf{x}_p) \phi_J(\mathbf{x}_p) \quad (2.32)$$

Note that, in the standard MPM, the mass matrix is not constant as in FEM. The external force vector is expressed as

$$f_I^{ext} = \sum_{p=1}^{n_p} m_p \phi_I(\mathbf{x}_p)(b)(\mathbf{x}_p) + \sum_{p=1}^{n_p} m_p \phi_I(\mathbf{x}_p)\bar{t}_i^s(\mathbf{x}_p)h^{-1} \tag{2.33}$$

While the internal force vector become

$$f_I^{int} = -\sum_{p=1}^{n_p} m_p/\rho\sigma_p \nabla\ \phi_I(\mathbf{x}_p) = -\sum_{p=1}^{n_p} V_p \sigma_p \nabla\ \phi_I(\mathbf{x}_p) \tag{2.34}$$

where the $V_p$ is the volume of particle $p$ ,note that, the particle density is the ratio of the particle mass to particle volume; $\nabla\ \phi_I = \left(\frac{\partial\phi_I}{\partial x_1}, \frac{\partial\phi_I}{\partial x_2}, \frac{\partial\phi_I}{\partial x_3}\right)^T$; $\sigma_p$ is the 3×3 Cauchy stress matrix of particle $p$.

To warm up, the derivation of the momentum weak form equation has been illustrated in Equation(2.31). Also, the MPM semi-discrete equation has been explained as described in[57].

# 3 MATERIAL POINT METHOD

## 3.1 Discretization and Material Point Method Algorithms

The time integration of the weak form equation (2.31) provides the full discretized solution of the MPM. In this section, the general MPM algorithms are illustrated.

### 3.1.1 Mass Matrix

Solving the nodal acceleration needs to apply a linear solution in each time step. This generates a large number of systems, especially in the MPM 3D model. Therefore, the lumped mass matrix is a good simplification method where it's a diagonal matrix system; thus, the diagonal terms in mass matrix can be written as

$$m_I = \sum_{I=1}^{n_n} m_{IJ} = \sum_{J=1}^{n_n} \sum_{p=1}^{n_p} m_p \phi_I(\mathbf{x}_p)\phi_J(\mathbf{x}_p) = \sum_{p=1}^{n_p} m_p \phi_I(\mathbf{x}_p) \tag{3.1}$$

Recall the FE shape functions property in which the summation of the shape function equal to one along x, $\sum_J \phi_J(\mathbf{x}) = 1$, so that provides the last form in the equation (3.1). conservation of mass at the nodes is also satisfied because the momentum equation is solved at the grid nodes; thus, the equation (3.1) is expressed as

$$\sum_I m_I = \sum_I \left( \sum_{p=1}^{n_p} m_p \phi_I(\mathbf{x}_p) \right) = \sum_{p=1}^{n_p} m_p \left( \sum_I \phi_I(\mathbf{x}_p) \right) = \sum_p m_p \tag{3.2}$$

Lumped mass matrix lead to provide the ordinary differential equations of equation (2.31) as

$$m_I \mathbf{a}_I(t) = \mathbf{f}_I(t) = f_I^{ext}(t) + f_I^{int}(t) \tag{3.3.A}$$

where the acceleration is given as

$$a_I = \frac{d\mathbf{v}_I(t)}{dt} \tag{3.3.B}$$

at all node I

The time domain $0 \geq t \geq t_f$ is divided to time steps $\mathbf{\Delta t} = t_f/n_T$ with time increments . To apply the solution in time, solving the semi-discrete equations provides an explicit formulation that increases the time with each time step from $t$ to $t+\mathbf{\Delta t}$ regardless the linear algebra equations. However, the explicit formulation must consider the use of small time steps $\mathbf{\Delta t}$ to satisfy the stability of the model.

In MPM, the node velocities are avoided after each time step when the node is in reset. Thereby, the particle velocities must be protruded to the nodes to provide a start point for the time increment. This extremely important step will be discussed in the next section.

### 3.1.2 Nodal Velocities Determination

The particle velocities must be protruded to the nodes at the beginning of each time step. Thus, the nodal momenta are mapped to the nodes by using the shape function as

$$(m\mathbf{v})_I^t = \sum_p \phi(\mathbf{x}_p^t)(m\mathbf{v})_p^t \tag{3.4}$$

Note that the use of superscript t is referred to the current time step t, which is a known value, while the superscript $t + \mathbf{\Delta t}$ refers to the next time step with an unknown value.

An important question should be raised by the reader, which velocity particle should be mapped to the node since the number of particles is larger than the number of nodes? The use of the least square approximation provides a suitable answer for this question. The least square approximation is considered the best approximation that reduces the difference between the exact function to the approximated one; thus, the quality of this approach can be measured by tracking the differences between the two mentioned functions.

## 3.2 Material Point Method Algorithms

### 3.2.1 Standard Formulation (USL)

The Updated Stress Last (USL) is considered the most common MPM algorithm. From the nodal acceleration equation $\mathbf{a}_I^t = \mathbf{f}_I^t / m_I^t$, the nodal velocity is obtained as

$$\mathbf{v}_I^{t+\Delta t} = \mathbf{v}_I^t + \Delta t \mathbf{a}_I^t \tag{3.5}$$

This is called Euler forward method where $\mathbf{v}_I^t$ is the nodal velocity in the current time step, which is known, $\Delta t$ is the time increment. While the new position of nodes is written as

$$\mathbf{x}_I^{t+\Delta t} = \mathbf{x}_I^t + \Delta t \mathbf{v}_I^t \tag{3.6}$$

The nodes' new positions can not be recognized because the grid would be reset at the beginning of the next time step. The updating of the node position is a continuous process until the grid is distorted or replaced.

After the grid is updated, the particle state will be updated using the grid velocities. All position, velocity, volume, deformation gradient, stress, etc., are updated from grid to particle. Different ways have been used to compute the particle velocities; for example, in the particle-in-cell (PIC), total grid velocity is used to find the particle velocity. However, in FLIP (The Fluid implicit Particle method), the grid velocity increments are used to find the particle velocity. Both ways can be expressed mathematically as

PIC: $\mathbf{v}_I^{t+\Delta t} = \sum_I \phi_I(\mathbf{x}_p^t)\mathbf{v}_I^{t+\Delta t}$,

FLIB: $\mathbf{v}_I^{t+\Delta t} = \mathbf{v}_p^t + \sum_I \phi_I(\mathbf{x}_p^t)[\mathbf{v}_I^{t+\Delta t} - \mathbf{v}_I^t]$,

while the position has been expressed mathematically as

$$\mathbf{x}_p^{t+\Delta t} = \mathbf{x}_p^t + \Delta t \sum_I \phi_I(\mathbf{x}_p^t)\mathbf{v}_I^{t+\Delta t} \tag{3.7}$$

Then, the particle stresses would be updated using the constitutive models. This update starts with determination of the deformation gradient **F**, the velocity gradient **L** and the deformation rate **D**. For the elastic body, the key step to update the stress is to obtain the particle velocity gradients, then determination of the deformation gradient $\dot{F} = LF$ and then compute the updated particle volume. This procedure can be expressed as

$$\mathbf{L}_p^{t+\Delta t} \equiv \nabla \mathbf{v}_p^{t+\Delta t} \mathbf{x}_p^t = \sum_I \nabla \phi_I(\mathbf{x}_p^t) \mathbf{v}_I^{t+\Delta t} \tag{3.8.A}$$

$$\frac{\mathbf{F}^{t+\Delta t} - \mathbf{F}^t}{\mathbf{\Delta t}} = \mathbf{L}^{t+\Delta t} - \mathbf{F}^t, \rightarrow \mathbf{F}_p^{t+\Delta t} = (\mathbf{I} + \mathbf{L}^{t+\Delta t} \Delta t)\mathbf{F}_p^t \tag{3.8.B}$$

$$V_p^{t+\Delta t} = J V_p^0, \quad \rightarrow J = det \mathbf{F}_p^{t+\Delta t} \tag{3.8.C}$$

$$\rho_p^{t+\Delta t} = \rho_0 / J \tag{3.8.D}$$

where $I$ is the Identity matrix,$\nabla$ is the gradient multiplier and $J$ is the determinant of the updated deformation gradient.

The strain increment is computed regarding to the hypo-elastic constitutive models. The aim is to use it to compute the stress increments; thus, the strain increment equation is written as

$$\Delta e_p = (\sum \mathbf{L}_p^{t+\Delta t}) \Delta t \tag{3.9}$$

while the updated particle stress equation is expressed as

$$\sigma_p^{t+\Delta t} = (\sigma_p^t + \Delta \ \sigma_p) \tag{3.10}$$

### 3.2.2 Modified Updated Stress Last (MUSL)

In this algorithm, Sulsky et al. [59] introduced a solution for the small mass issue. After mapping the nodal velocities to the particle, the updated particle velocities are mapped back to the nodes to provide nodal velocities as

$$(m\mathbf{v})_I^{t+\Delta}t = \sum_p \phi_I(\mathbf{x}_p)(m\mathbf{v})_p^{t+\Delta t} \tag{3.11}$$

So, the nodal velocity become

$$\mathbf{v}_I^{t+\Delta t} = \frac{(m\mathbf{v})_p^{t+\Delta t}}{m_I^t} = \frac{\sum_p \phi_I(\mathbf{x}_p)(m\mathbf{v})_p^{t+\Delta t}}{\sum_p \phi_I(\mathbf{x}_p)m_p} = \frac{\sum_p \phi_I(\mathbf{x}_p)(m\mathbf{v})_p^{t+\Delta t}}{m_I^t} \tag{3.12}$$

The shape functions are occupied in the numerator and denominator; therefore, the shape functions role disappears. As a result, this cancellation solves the issue of the large velocity gradient in the USL. This method is also called the double mapping USL as the momenta is mapped at the beginning of each time step and after the update of nodal velocity. This algorithm is adopted in this research for the MPM analysis.

### 3.2.3 Total Lagrangian Material Point method (TLMPM)

Background

Mesh-less methods represent appropriate concepts to simulate large deformation problems in solid mechanics compared to mesh-based methods. However, Mesh-less methods consist of instability issues and numerical fracture. Thus, such methods could not perform accurately for analyzing engineering problems such as machining, wear, and impacts where the damage and fracture appear[9]. Total- Lagrangian (TL) particle-based methods show resistance to the numerical fracture due to the stability of the background grids of the reference configuration through the analysis. The Total-Lagrangian material point method could be used for the same reason; it was introduced by Steffen et al. [55] to study the convergence of the standard MPM. Further, it was used for graphic simulation by Zhu et al. [65].

Currently, the Total-Lagrangian material point method of solid mechanics undergoing large deformation was developed by deVaucorbeil et al. [9] for the first time. Convergence study of the Total-Lagrangian material point method was also examined based on the Method of

**Algorithm 1** MUSL analytical procedure

**procedure** SULSKY ET AL([59])
    Model Initialization
    Discertize the Cartesuan grid, set time t=0
    Read the particle data: $\mathbf{x}_p^0$, $\mathbf{v}_p^0$, $\sigma_p^0$,$\mathbf{F}_p^0$, $\mathbf{V}_p^0$, $\mathbf{m}_p$,$\rho_p^0$
    **end**
    **while** $t < t_f$ do:
    Initialize the grid quantities: $m_I^t = 0$, $(\mathrm{m}\mathbf{v})_I^t = 0$, $\mathbf{f}_I^{ext} = 0$, $\mathbf{f}_I^{int} = 0$.
    Mapping from particle to nodes
        Compute nodal mass: $m_I^t = \sum_p \phi(\mathbf{x}_p^t) m_p$
        Compute nodal momentum: $(m\mathbf{v})_I^t = \sum_p \phi(\mathbf{x}_p^t)(m\mathbf{v})_p^t$
        Compute external force: $f_I^{ext,t} = \sum_p \phi(x_p) m_p \mathbf{b}(\mathbf{x}_p)$
        Compute external force: $f_I^{int,t} = -\sum_p V_p^t \sigma_p^t \nabla\phi(x_p^t)$
        Compute nodal force: $f_I^t = f_I^{ext,t} + f_I^{int,t}$
    **end**
    **Update the momenta** $(m\mathbf{v})_I^{t+\Delta t} = (m\mathbf{v})_I^t + f_I^t \Delta t$
    **Fix the nodes corresponding to the boundary conditions** $(m\mathbf{v})_I^{t+\Delta t} = 0$ and $(m\mathbf{v})_I^t = 0$
    **Update particle velocities and grid velocities (double mapping)**
        Compute nodal velocities: $\mathbf{v}_I^{t+\Delta t} = (m\mathbf{v})_I^{t+\Delta t} / m_I^t$
        Update the particle positions: $\mathbf{x}_p^{t+\Delta t} = \mathbf{x}_p^t + \ \mathbf{v}_I^{t+\Delta t} \Delta t$
        Update the particle velocities: $\mathbf{v}_p^{t+\Delta t} = \mathbf{v}_p^t + \mathbf{a}_p^t \Delta t$
        Update the grid velocities:$(m\mathbf{v})_I^{t+\Delta t} = \sum_p \phi(\mathbf{x}_p^t)(m\mathbf{v})_p^{t+\Delta t}$
        Fix the Dirichlet nodes: $(m\mathbf{v})_I^{t+\Delta t} = 0$
    **end**
    **Updated particles**
        Compute nodal Velocities: $\mathbf{v}_I^t = (m\mathbf{v})_I^t / m_I^t$
        Compute the gradient velocity: $\mathbf{L}_p^{t+\Delta t} = \sum_I \nabla\phi_I(\mathbf{x}_p^t)\mathbf{v}_I^{t+\Delta t}$
        Update the gradient deformation: $\mathbf{F}_p^{t+\Delta t} = (\mathbf{I} + \mathbf{L}^{t+\Delta t}\Delta t)\mathbf{F}_p^t$
        Update the volume : $V_p^{t+\Delta t} = J V_p^0, \rightarrow J = \det \mathbf{F}_p^{t+\Delta t}$
        Update the stress: $\sigma_p^{t+\Delta t} = (\sigma_p^t + \Delta\ \sigma_p)$
    **end**
    **Next time step** = t+ $\Delta$t
    **end while**

Manufactured Solution. Applications subjected to large deformation have been presented for the vibration of the compliant bar subjected to the gravity field and Taylor bar impact test. The presented Total-Lagrangian material point method (TLMPM) is not similar to the

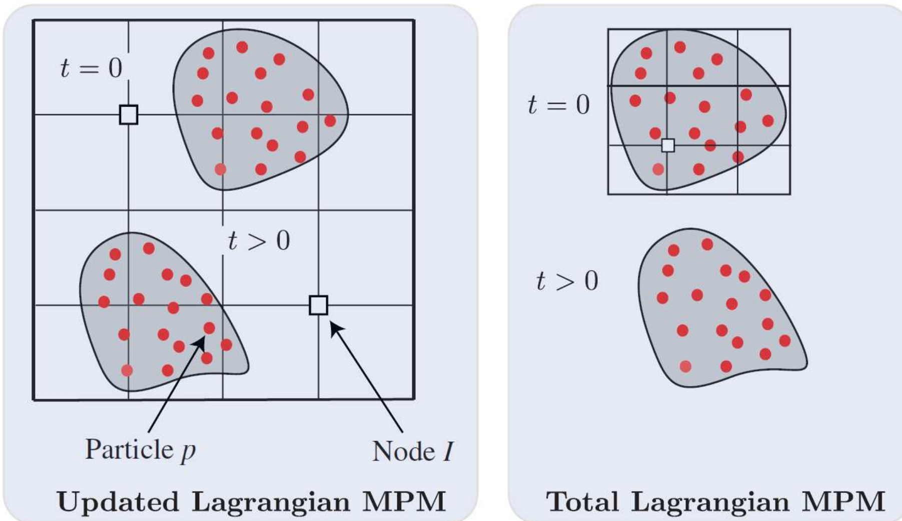


Figure 3: Difference betweem ULMPM and TLMPM (Retrieved from [10])

Total-Lagrangian finite element method (TLFEM) since the TLMPM does not represent a conforming mesh that allows analysis of the extremely large deformation problems.

Based on the Lagrangian formulation concept, two independent variable refer to the reference configuration are the material coordinate $\boldsymbol{X}$ and time $\boldsymbol{t}$. In the Total-Lagrangian material point method, the stress and strains components are introduced based on the reference configuration. Thus, the integration of the weak form is established with respect to the reference configuration. The material coordinate in the current configuration $\boldsymbol{x}$ can be presented in terms of the displacement $\boldsymbol{u}$ as

$$\boldsymbol{x} = \boldsymbol{u} + \boldsymbol{X} \tag{3.13}$$

The Total-Lagrangian conservation equation is given as

$$\rho = J\rho_0 \tag{3.14}$$

$$\frac{\partial \boldsymbol{v}}{\partial t} = \frac{1}{\rho_0} \nabla_0 \cdot \boldsymbol{P}^T + \boldsymbol{b} \tag{3.15}$$

where the $\boldsymbol{v}$ velocity field, $\rho$ is the mass density, $\boldsymbol{P}$ is the first Piola–Kirchhoff stress tensor, $\mathbf{b}$ are the external forces, $\nabla_0$ is the gradient operator where is applied with respect to the reference configuration and $J$ is the determinant of the deformation gradient $\boldsymbol{F}$ that is presented as:

$$\boldsymbol{F} = \frac{\partial \boldsymbol{x}}{\partial \boldsymbol{X}} = \frac{d\boldsymbol{u}}{d\boldsymbol{X}} + \boldsymbol{I} \tag{3.16}$$

In the current Total-Lagrangian material point method (TLMPM), The procedure is almost identical to the standard MPM. The differences can be represented in 1) the $1^{st}$ PK stress is applied in the internal forcing function, 2) the spatial derivatives are in terms of the material coordinate $\mathbf{X}_p$, 3) different deformation gradient and velocity gradient computational approaches are adopted in TLMPM. Algorithms 2 represents the TLMPM procedure developed by [9].

## 3.3 Shape Functions of MPM

The previous sections discussed the general framework of the MPM. However, the shape functions have not been decided yet. Different shape functions were examined with MPM formulations as; 1)Linear Lagrange functions, 2)Generalized interpolation MPM, 3) B-splines, 4) Bernstein functions. Note that the discussion here is specified to the Cartesian grid for the linear shape function adopted in this research.

### 3.3.1 Shape Functions Properties

Any shape functions $\phi(x)$ should be continuous along the grid's boundaries. In addition, they should meet the listed properties as

**1. Partition of Unity** $\sum_I \phi_I(x) = 1$ along all x.

**Algorithm 2** TLMPM analytical procedure

**procedure** DE VAUCORBEIL ET AL([9])
  Model Initialization
  Read the particle data: $\mathbf{x}_p^0$, $\mathbf{v}_p^0$, $\sigma_p^0$,$\mathbf{F}_p^0$, $\mathbf{V}_p^0$, $\mathbf{m}_p$,$\rho_p^0$
  Compute nodal mass: $m_I^t = \sum_p \phi(\mathbf{x}_p^t) m_p$
  Compute and store the shape function and the derivatives: $\phi_I(X_p)$and$\nabla_0\phi_I(X_p)$ ▷ For undeformed configuration
  **end**
  **while** $t < t_f$ do:
  Reset the grid quantities: $m_I^t = 0$, $(\mathrm{m}\mathbf{v})_I^t = 0$, $\mathbf{f}_I^{ext} = 0$, $\mathbf{f}_I^{int} = 0$.
  Mapping from particle to nodes
    Compute nodal momentum: $(m\mathbf{v})_I^t = \sum_p \phi(\mathbf{x}_p^t)(m\mathbf{v})_p^t$
    Compute external force: $f_I^{ext,t}$
    Compute external force: $f_I^{int,t} = -\sum_{p=1}^{n_p} V_p^o \mathbf{P}_p^t \nabla\phi(\mathbf{X}_p)$
    Compute nodal force: $f_I^t = f_I^{ext,t} + f_I^{int,t}$
  **end**
  **Update the momenta** $(m\mathbf{v})_I^{t+\Delta t} = (m\mathbf{v})_I^t + f_I^t \Delta t$
  **Fix the nodes corresponding to the boundary conditions** $(m\mathbf{v})_I^{t+\Delta t} = 0$ and $(m\mathbf{v})_I^t = 0$
  **Update particle velocities and grid velocities (double mapping)**
    Compute nodal Velocities: $\mathbf{v}_I^t = (m\mathbf{v})_I^{t+\Delta t}/m_I^t$
    Update the particle positions: $\mathbf{x}_p^{t+\Delta t} = \mathbf{x}_p^t + \mathbf{v}_I^{t+\Delta t}\Delta t$
    Update the particle velocities: $\mathbf{v}_p^{t+\Delta t} = \mathbf{v}_p^t + \mathbf{a}_p^t \Delta t$
    Update the grid velocities:$(m\mathbf{v})_I^{t+\Delta t} = \sum_p \phi(\mathbf{X}_p)(m\mathbf{v})_p^{t+\Delta t}$
    Fix the Dirichlet nodes: $(m\mathbf{v})_I^{t+\Delta t} = 0$
  **end**
  **Updated particles**
    Compute $\dot{F}_p^{t+\Delta t} = \sum_I \nabla\phi(\mathbf{X}_p)\ \mathbf{v}_I^{t+\Delta t}$
    Update the gradient deformation: $\mathbf{F}_p^{t+\Delta t} = \mathbf{F}_p + \Delta t \dot{F}_p^{t+\Delta t}$
    Compute the gradient velocity: $\mathbf{L}_p^{t+\Delta t} = \dot{F}_p^{t+\Delta t}(\mathbf{F}_p^{t+\Delta t})^{-1}$
    Update the stress: $\sigma_p^{t+\Delta t} = (\sigma_p^t + \Delta\sigma_p)$
    convert stresses to $1^{st}$ PK stresses: $\mathbf{P}_p^{t+\Delta t} = g(\sigma_p^{t+\Delta t})$
    Updated particle position : $\mathbf{x}_p^{t+\Delta t} = \mathbf{x}_p^t + \Delta t \sum_I \phi(\mathbf{X}_p)\mathbf{v}_I^{t+\Delta t}$
  **end**
  **end while**

2. **Compact support** $\phi_I(x) \neq 0$ to the particle that close to node $I$.

3. **Positive shape functions** $\phi_I(x) \geq 0$ for all x.

4. **Kronecker delta property** $\phi_I(x_J) = \delta_{IJ}$.

### 3.3.2 Linear Lagrangian Function

Consider 1D element, the shape function are defined as

$$N_I^x(x) = \begin{cases} 1 - \left|x - x_I\right|/h_x, & \text{if } \left|x - x_I\right| \leq /h_x \\ 0, & \text{else} \end{cases} \tag{3.17}$$

where $h_x$ is the element length in $x$ direction. Note that The shape functions are defined in the global coordinates system. While their derivatives are defined as

$$N_{I,x}^x(x) \equiv \frac{dN_I^x(x)}{dx} = \begin{cases} 1 - sign(x - x_I)|/h_x, & \text{if } \left|x - x_I\right| \leq /h_x \\ 0, & \text{else} \end{cases} \tag{3.18}$$

In a 2D element, the shape function is the tensor- product of two shape functions in the x and y directions which can be given as

$$N_I(x, y) = N_I^x(x)N_I^y(y) \tag{3.19}$$

This shape functions 'hat functions' used in the standard MPM formulation.

# 4 BEAMS MECHANICS ANALYSIS USING THE MATERIAL POINT METHOD

## 4.1 Linear Beams Mechanics Analysis

### 4.1.1 Introduction and Literature Review

After establishing the elasticity equations that reflect the kinematics constraints and linear deformation theory 'small deformation' as well as the stress field that generalized the equilibrium equations in the linear elastic solid, the response of the materials takes place to complete the general formulation of the elasticity solutions under linear deformation concept which usually known as "linear elastic material." This theory is related to the description of the physical properties and relating them under the "constitutive equations" concept. Due to the limitation of the materials and loading cases, the generalization of the constitutive equations is one of the most important concepts in mechanics.

The most important contributions to the elasticity solution were made by 1) Timoshenko and Goodier [61] they introduced the elasticity solutions to engineering problems. Both focused on the limited produced deformation due to the external loads. Also, the bodies that were studying assumed to have the same properties in the different directions "isotropic." 2) While the anisotropic plate was investigated by Lekhintskii [28]. 3) Exact solution of composite laminates has been studied by Pagano [44]. The author considered the classical laminates plate theory in the investigation compared to the elasticity solutions with different boundary values problems.

For beams investigations, Gere and Timoshenko[17] studied the beams for fixed ends undergoing uniform load conditions using the Euler-Bernoulli beam theory. Later, the elasticity of variable-arc- length beams subjected to the end moment was studied by chucheepsahul, Bunacharoen and Huang [8]. The examiners considered the large deformation as the basis of this research. The method yields the exact solution with results compared to finite element analysis and linear theory showing good agreements. In addition, functionally graded (FG) beams subjected to transverse load have been studied by B.V. Sankar [53]. The author assumed the effect of the Poisson ratio is held constant. A slender beam theory, "Euler - Bernoulli beam theory," was considered in this analysis. The author validated the FG beam theory for Euler- Bernoulli when the transverse load varies slowly. Also, the static response of simply supported functionally graded plate has been analyzed. Based on the third-order shear theory, the results obtained were compared with the result of the finite point multiquadric method[16]. Ding et al. [13] analyzed the different fixed end beams conditions: cantilevered beam, propped-cantilevered beam, and fixed ends beam using stress functions. The study has been done considering different material properties: isotropic and anisotropic beams. Also, they expanded the analysis to include the functionally graded beam in this investigation sets[12].

Eer Nisse[14] purposed one of the earliest analyses of linear vibration for piezoelectric desk investigation. The direct approximation method has been used for formulation. The results show excellent agreements for natural frequencies and mode shapes with different approximation solutions. Later, OHNO [41] studied the free vibration of parallelepiped rectangular crystal based on Demarest's cube resource theory. Later, Heyliger and Al Jilani [21] examined the free vibration of cylinders and spheres using Ritz approximation. Three different coordinate systems were adopted in this research. The results compared with other approaches were in remarkable agreement. While Reddy[49] used various beam theories to formulate the nonlocality approach. Then, Ma et el. [33] extended the analysis to include the Timoshenko beam theory of dynamic response. Their model produces natural frequencies larger than the classical model. Poisson ratio impact is considered and plays a role in natural frequency values. Also, the size effect has been examined and has a noticeable effect on the results. Functionally graded beams with vibrating boundary conditions were introduced by Mesut[24] Both Lagrange equation and Lagrange multipliers were used to formulate the equations of frequencies and the boundary conditions, respectively. Aluminum and alumina beam-type materials were used in this analysis. As the slenderness ratio increases, the higher frequency values are increased.

A comparison of the material point method (MPM) with the elasticity solutions has been completed by S.Andersen and L.Andersen [3]. The investigations considered different simple-linear elastic problems including the cantilevered beam subjected to the transverse point load in the end. The result shows as the order of the used interpolations increases, the error to the elasticity solutions is reduced. A quasi-static material point method formulation was validated by Beuth et al. [7] for the cantilevered beam model and the results were compared to the finite element method.

The material point method was developed about 25 years ago. The method is used in the formulation of continuum mechanics problems. Continuum mechanics concepts generally are well-known in modeling solids and fluids at macroscopic scales considering the homogenizes. Thus, the smooth functions of spatial variables can determine solids and fluids behaviors. In continuum mechanics, four significant aspects are included; 1) motion and deformation as known as "Kinematics", 2) the impact of the internal forces that are related to the applied external conditions "kinetics", 3) the conservation equations which allow the physical properties to be introduced and stored like; mass, momentum and energies and 4) the constitutive equations that describe the relationship between the kinematics and the kinetics. In the MPM, The continuum can be represented by a set of the material particles that are tracked through the calculation, while the background grids are used to solve the continuum equations [10].

The earliest material point method (MPM) solid mechanics applications were introduced by and Sulsky et al. [57, 59] in the formulation of the dynamic and impacted behavior of cylinders and spheres. The first representation of the axial vibration of continuum bar analysis was developed by S.Andersen and L.Andersen [3]. Later, de Vaucorbeil et al. [9] examined the nonlinear formulation on the extended bar under large deformation.

### 4.1.2 Static Bar Analysis

The aim is to generate the bar axial displacement that performs in the generated stress and the bar stiffness. The material point model of the case of the axially loaded bar is established, however, to analyze a static model in the MPM dynamic framework, the load is applied with increasing in time increments, whereas the boundary conditions are imposed on the related velocity nodes variable. Thus, the particle's position would be followed through each time step to the end of the simulation. The updated particles' strain can be tracked in the two directions (x and y) to examine the influence of the Passion's ratio in the static response, which is mainly a ratio of the transverse strain to the axial strains.

The proposed material point model starts to solve the axially loaded bar behavior and validates its outcomes with the linear elasticity solution based on the plane-stress concept, where the stress components out of the plane are equal to zero. Depending on the fourth-order elastic tensor $\mathbf{C}$, the in-plane stress components are function of the elasticity module $\mathbf{E}$ and the Poisson ratio parameters $\boldsymbol{\nu}$. Small deformation analysis was adopted to validate the result with the linear elasticity solution. The normal component of stress was taken as

$$\sigma_{xx} = \frac{P}{A} \tag{4.1}$$

while the strain component in y direction is computed as

$$\epsilon_{yy} = \frac{\nu * \sigma_{xx}}{E} \tag{4.2}$$

In the material point model, the two-dimensional four nodes elements were considered for representing each background cell over the entire domain $\mathbf{\Omega}$. The entire domain is discretized by a set of material sub-domains $\boldsymbol{\Omega_p}$ in which the total mass of the sub-domain is assumed to be carried by the material point. Every background cell has nodes $\boldsymbol{n_n}$ with shape function

$\boldsymbol{\phi_I}$ corresponding for every node **I**. The evaluation of the shape functions and derivatives is identical to the finite element analysis, which does not include neighbor search as other mesh-free methods. The linear interpolation function was used in the analysis based on the location of each particle, which allows the particles' information to transform to the nodes.

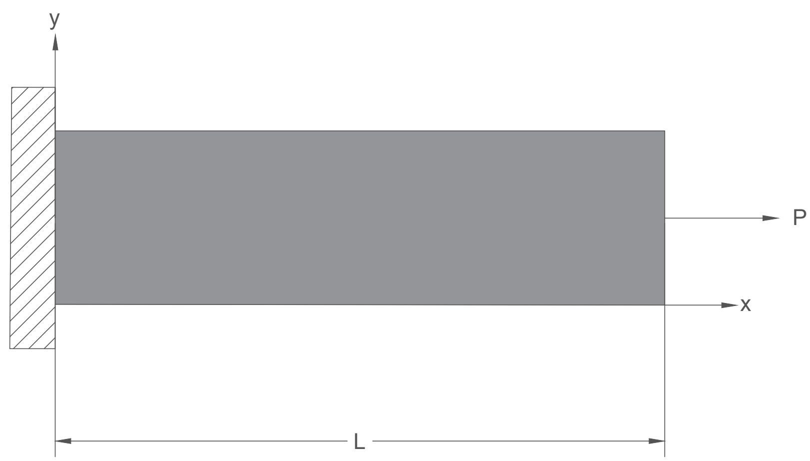


Figure 4: The bar geometry

The bar geometry is shown in Figure 4 with the length $L = 8\ m$, the height $h = 1\ m$, and the modulus of elasticity $E = 3 \times 10^5\ Gpa$. The bar meshed to the 8 elements with 192 embedded material points. To simulate the behavior, the left end boundary conditions have been imposed considering the nodal velocity values equal to zero. The external force assumption has been applied directly to the nodes in the background cell. The resulted axial displacement was in excellent agreement with the analytical solution for various applied loads.

Passion's ratio influence was examined using the material point model. Unlike other approximated methods, the strain increments of each particle can be tracked for a time step in which provides a known variable to the constitutive equation. Thus, by assuming a Passion's ratio $\nu = 0.3$, the material point model generated transverse strains that accomplished excellent agreements with the elasticity solution. However, a slight reduction for axial displacements in compersion to the analytical solution was notable due to the change in the bar stiffness. Table 2 and Table 3 show the axial particle displacements and the transverse strain results for different applied loads at $\nu = 0.0$ and $\nu = 0.3$ , respectively.

Table 2: Bar axial displacements and strains, $\nu = 0.0$

| | | Elasticity | | MPM | |
|---|---|---|---|---|---|
| load (P) | PL/AE | $\Delta_{xx}$ | $\epsilon_{yy}$ | $\Delta_{xx}$ | $\epsilon_{yy}$ |
| 10 | 0.00027 | 0.0002667 | 0.00 | 0.0002728 | 0.00 |
| 20 | 0.00053 | 0.0005333 | 0.00 | 0.0005455 | 0.00 |
| 30 | 0.00080 | 0.0008000 | 0.00 | 0.0008182 | 0.00 |
| 40 | 0.00107 | 0.0010667 | 0.00 | 0.0010908 | 0.00 |
| 50 | 0.00133 | 0.0013333 | 0.00 | 0.0013632 | 0.00 |
| 60 | 0.00160 | 0.0016000 | 0.00 | 0.0016356 | 0.00 |
| 70 | 0.00187 | 0.0018667 | 0.00 | 0.0019080 | 0.00 |
| 80 | 0.00213 | 0.0021333 | 0.00 | 0.0021802 | 0.00 |
| 90 | 0.00240 | 0.0024000 | 0.00 | 0.0024523 | 0.00 |
| 100 | 0.00267 | 0.0026667 | 0.00 | 0.0027700 | 0.00 |

#### 4.1.3 Dynamic Bar Analysis

To study the dynamic behavior of the material point method, the axial vibration of a continuum of two-dimensional bar considered with length $L = 10\ m$, the height $h = 1\ m$, and the modulus of elasticity $E = 10000\ Gpa$. This test is an extension of the one-dimensional analysis that was done by Bardenhagen [4]. The one-dimensional analysis was done based on both Updated Stress Last (USL) and Modified Updated Stress Last (MUSL) formulations.

Table 3: Bar axial displacements and strains, $\nu = 0.3$

| | | Elasticity | | MPM | |
|---|---|---|---|---|---|
| load (P) | PL/AE | $\Delta_{xx}$ | $\epsilon_{yy}$ | $\Delta_{xx}$ | $\epsilon_{yy}$ |
| 10 | 0.00027 | 0.0002427 | -0.000009 | 0.0002421 | -0.000008 |
| 20 | 0.00053 | 0.0004853 | -0.000018 | 0.0004846 | -0.000016 |
| 30 | 0.00080 | 0.0007280 | -0.000027 | 0.0007275 | -0.000025 |
| 40 | 0.00107 | 0.0009707 | -0.000036 | 0.0009708 | -0.000034 |
| 50 | 0.00133 | 0.0012133 | -0.000046 | 0.0012144 | -0.000043 |
| 60 | 0.00160 | 0.0014560 | -0.000055 | 0.0014585 | -0.000052 |
| 70 | 0.00187 | 0.0016987 | -0.000064 | 0.0017029 | -0.000061 |
| 80 | 0.00213 | 0.0019413 | -0.000073 | 0.0019478 | -0.000071 |
| 90 | 0.00240 | 0.0021840 | -0.000082 | 0.0021930 | -0.000080 |
| 100 | 0.00267 | 0.0024267 | -0.000091 | 0.0024387 | -0.000090 |

Here, in this analysis, the (MUSL) with consideration of the FILB approach, is adopted as described in algorithm 1. The outcomes were compared to the exact solution of

$$u(x,t) = \frac{v_0}{\omega_n} sin(\omega_n t) sin(\beta_n x) \tag{4.3}$$

$$v(x,t) = v_0 cos(\omega_n t) sin(\beta_n x) \tag{4.4}$$

where $\omega_n = \beta_n c$. The wavelength is given by $c = \sqrt{\frac{E}{\rho}}$. In the analysis, the initial velocity is given as $t$=0 as

$$v(x,0) = v_0 sin(\beta_n x) \tag{4.5}$$

The amplitude $v_0$ was taken as 0.1 since the analysis used linear interpolation functions. First mode analysis was considered in this example. Various material point discretization has been applied to examine the influence of the point sizes. The result shows some erroneous occurred as the minimum material points were applied. However, The MPM appears in excellent agreement with the analytical solution when the mesh becomes fine, as given in Figures 5 and 6. Thus, the linear shape functions perform excellently under the MPM formulation.

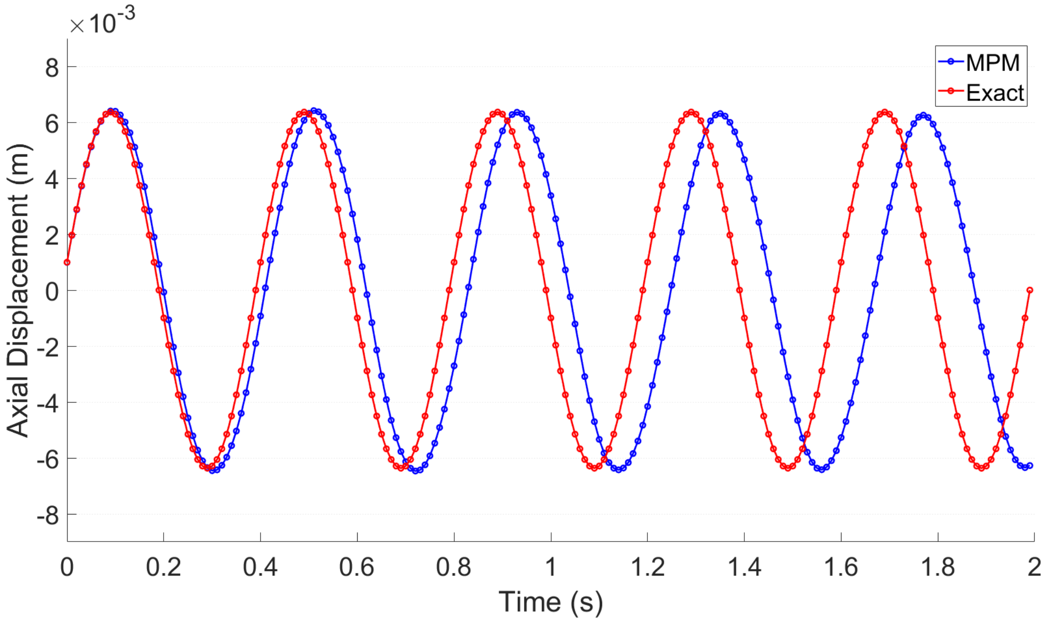


(a) Mesh 10x1

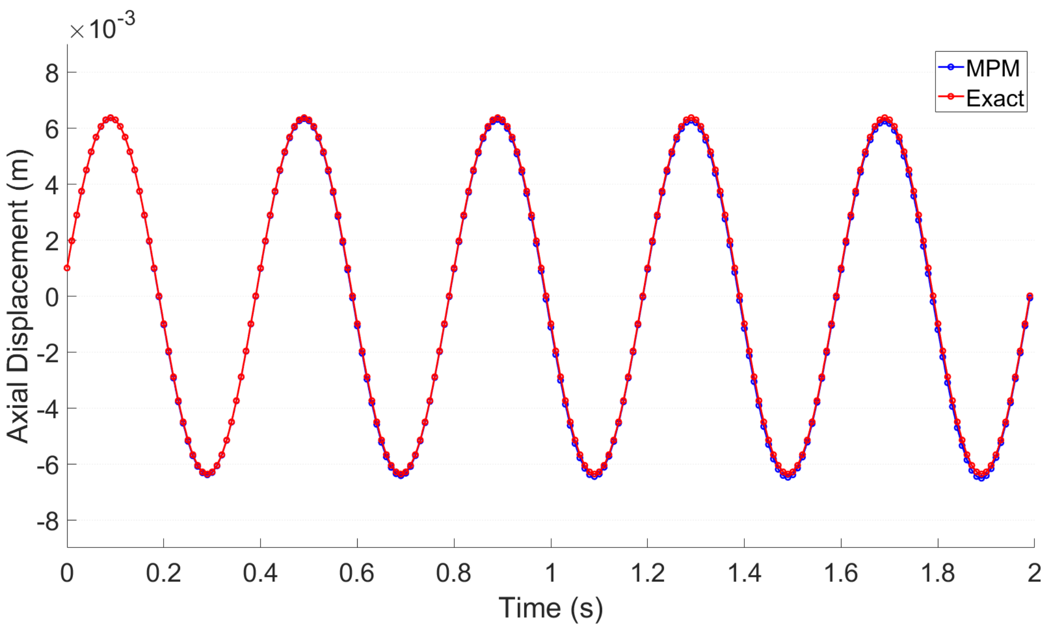


(b) Mesh 20x4

Figure 5: Axial displacement of cantilevered bar

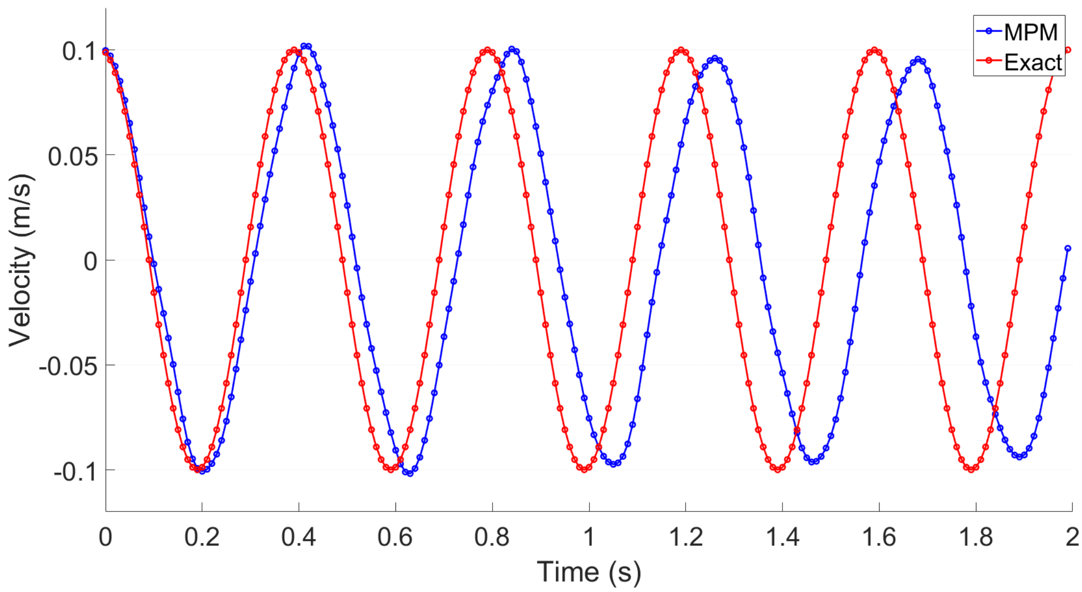


(a) Mesh 10x1

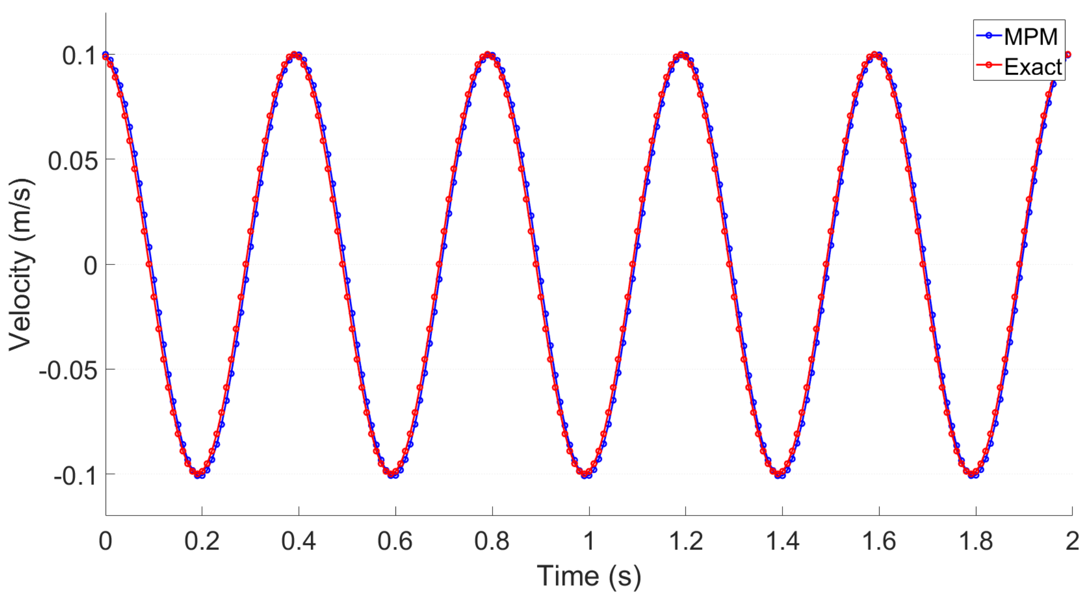


(b) Mesh 20x4

Figure 6: Particle velocity of cantilevered bar

Table 4: Transverse deflection of the end of cantilever beam

| Analytical solution[61] | MPM 16 | MPM 32 |
|---|---|---|
| -0.683 | -0.787 | -0.681 |

#### 4.1.4 Static Cantilevered Beam Analysis

The material point method was used here to find the transverse deflection of a cantilevered beam and compare it to the linear elasticity solution introduced by Timoshenko and Goodier [61]. The beam geometry is shown in Figure 7 with length $L = 8\ m$, the height $h = 1\ m$ , and the modulus of elasticity $E = 3000\ Gpa$. The beam deformation field has meshed to the 32 elements with 16 and 32 embedded material points over the beam domain, respectively. To simulate the behavior, the left end boundary conditions have been imposed considering the nodal resultant force values equal to zero. To study the static behavior using the dynamic framework of the material point method, the load has been gradually increased in each time step in which the external force assumption has been applied directly as a particle acceleration. The analysis started by solving the linear-elastic behavior of the beam to track the transverse deflection of a selected particle in each time step. To validate the result with the linear elasticity solution, the beam was assumed to be subjected to a small load value during the analysis. Imposing the boundary conditions was done by two assumptions were; 1) considering the vertical and axial components of the left end are fixed and 2) fixing the vertical component of the center of the left end and the components of the axial nodes. Both assumptions show convergence of the material point model with the analytical solution.

Figure 9 shows the deflection at the end of the beam. The behavior is obtained at $t = 4.44$. For the 16 material points model, the tip deflection gave larger displacement in comparison to the exact solution while the result appears a remarkable convergence when the martial points increased to 32 at the beam tip, as given in Table 4

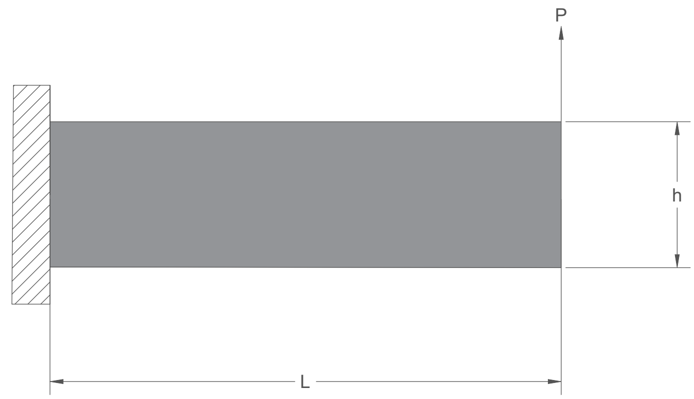


Figure 7: Geometrical description of the cantilevered beam

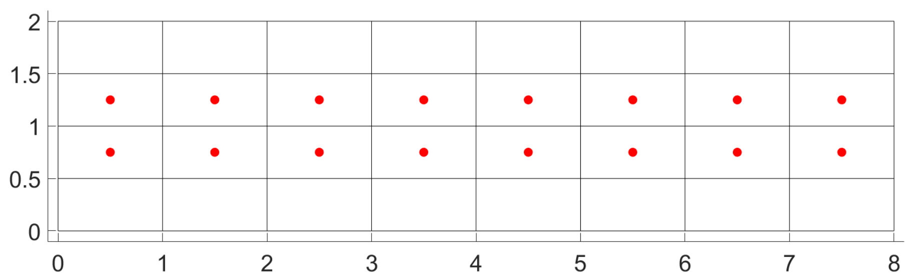


Figure 8: Initial MPM mesh of cantilever beam

#### 4.1.5 Static Simply Supported Beam Analysis

Simply supported beam analysis was studied. The beam is assumed to be subjected to the uniformly distributed load along its length. The model can track the transverse deflection of each particle. Further, the convergence study of the number of impeded particles has been examined in this analysis. The results show that as the number of particles increases, the convergence to the analytical solution increase, as shown in Table 5. The beam geometry is as same as the cantilevered beam model with length $L = 8\ m$, the height $h = 1\ m$, and the modulus of elasticity $E = 3000\ Gpa$. The beam deformation field meshed to the 32 elements with 16, 32, and 64 embedded material points over the beam domain, respectively. To simulate the behavior, the left and right ends have been imposed considering the nodal

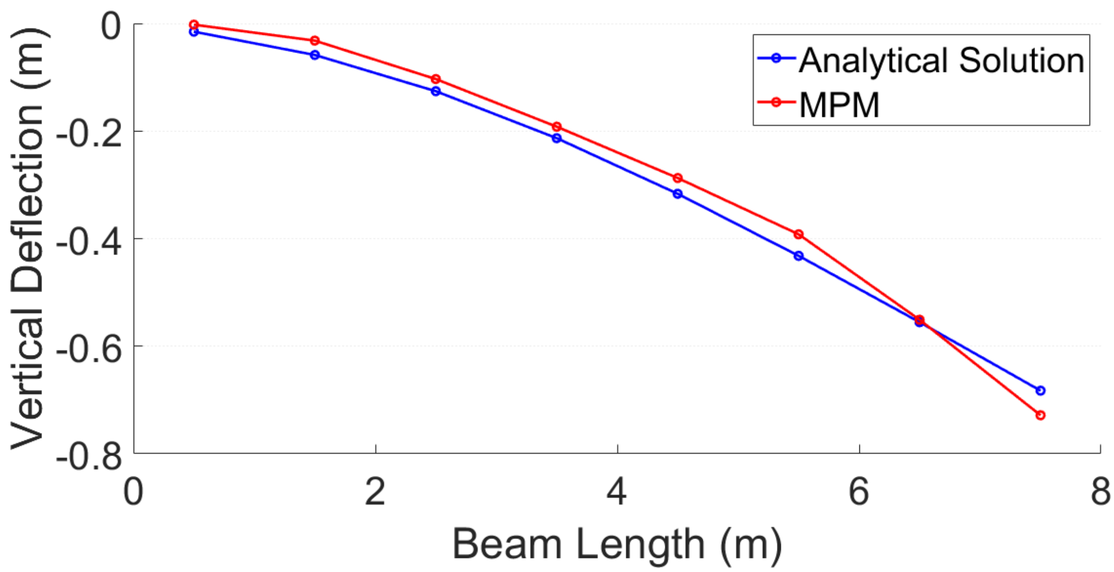


(a) MPM 16

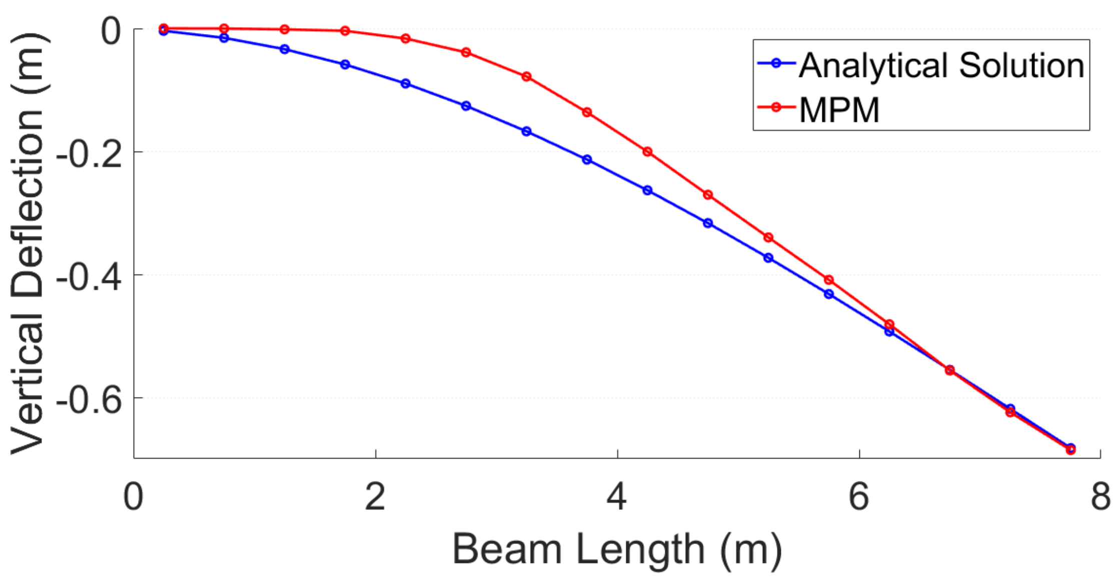


(b) MPM 32

Figure 9: Cantilevered beam deflection compared with analytical solution

Table 5: Transverse deflection at the middle of simply supported beam

| Analytical solution | MPM 16 | MPM 32 | MPM 64 |
|---|---|---|---|
| -0.212 | -0.333 | -0.346 | -0.206 |

resultant force values equal to zero. The external uniformly distributed load has been applied directly as accelerations for the upper particles along the beam. The results compared to the analytical deflection of the Euler-Bernoulli beam that is given by

$$\Delta_y = \frac{wx}{24EI}(l^3 - 2lx^2 + x^3) \tag{4.6}$$

The total load is also was taken as 1 with very small increments in each iteration. Figure 11 shows the average vertical deflection of the particles at the center of the cross-section along the beam length. Also, in the analysis, the load was increased as time function as described in Figure 11.b.

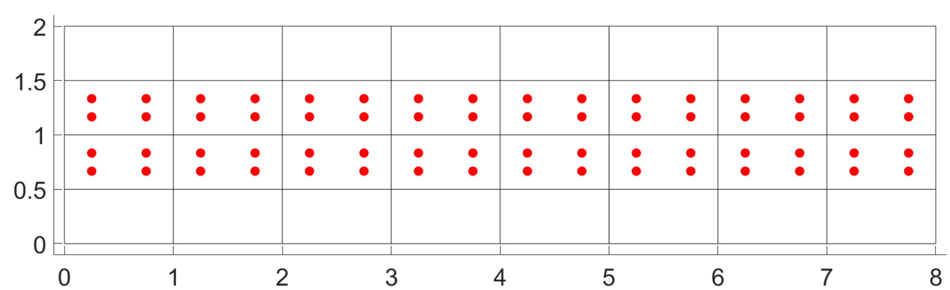


Figure 10: MPM mesh of simply supported beam with 64 points

### 4.1.6 Forced vibration of Cantilever Beam

To run a dynamic behavior, a cantilever beam analysis was adopted. The beam is assumed to be subjected to a harmonic force function. This force function was applied as an external

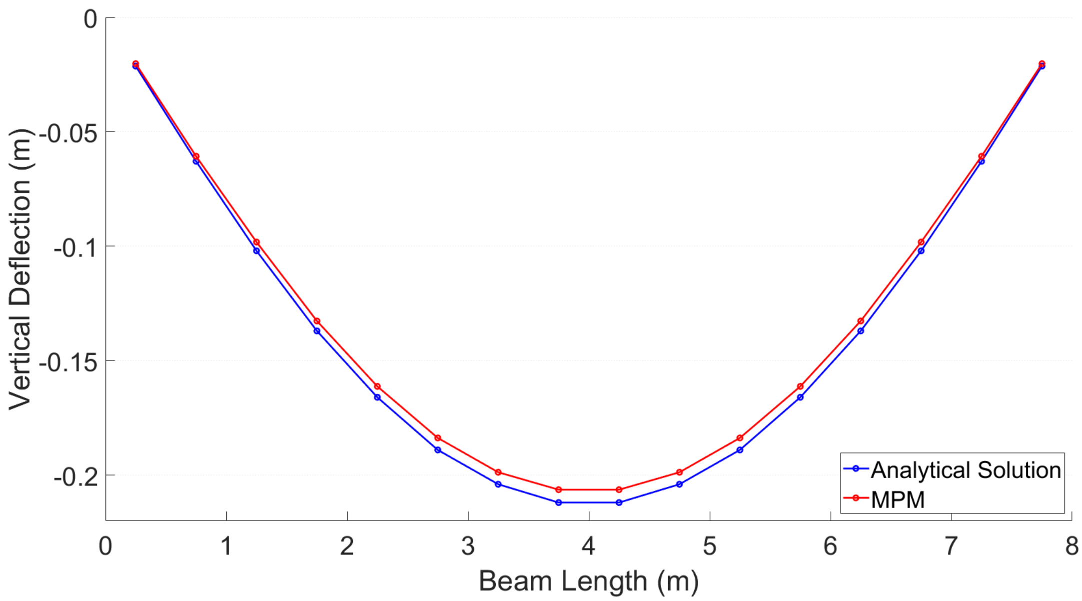


(a) MPM result with analytical solution

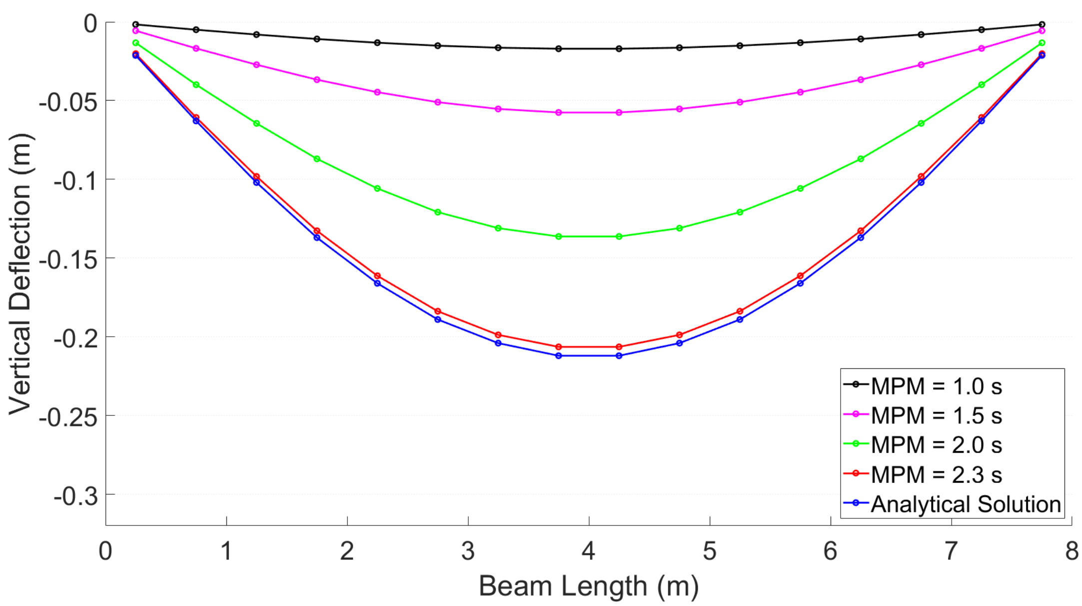


(b) MPM results at different time period

Figure 11: Vertical deflection of simply supported beam

force located at the end nodes of the beam. The force function is given by

$$f(t) = Fsin(\omega t) \tag{4.7}$$

Where F is the assumed amplitude taken as 0.002 in this analysis and $\omega$ is the forcing frequency. Weaver [62] interceded the steady-state response of the cantilever beam as

$$w(x,t) = \frac{Fl^3}{EI}\sum_{i=1}^{\infty}\frac{\beta_i X_i (X_i)_{x=l}}{(k_i l)^4} sin(\omega t) \tag{4.8}$$

Where $\beta_i$ are the magnification factors and $k_i l$ are the roots of the system frequency equation while $X_i$ are the characteristic functions representing the normal modes of beam vibration. From equation (4.8), the vertical velocity at the free end is given as

$$v(x,t) = \frac{4Fl^3\omega}{EI}\sum_{i=1}^{\infty}\frac{\beta_i}{(k_i l)^4} cos(\omega t), \tag{4.9}$$

after replacing the roots of the frequency equation, equation (4.9) can be rewritten as

$$v(x,t) = \frac{4Fl^3\omega}{EI}\left[\frac{\beta_1}{1.8751^4} + \frac{\beta_2}{4.6941^4} + ...\right] cos(\omega t) \tag{4.10}$$

The beam has the same geometric assumptions as of the static bar analysis with length $L = 10\ m$, the height $h = 1\ m$, the modulus of elasticity $E = 10000\ Gpa$ , and $\nu = 0.3$ . The analysis considered studying the dynamic behavior of the beam under the effect of the first three modal frequencies. To get the frequency for the MPM model, various forcing (driving) frequencies have been applied to track the amplitude of the particles near the end of the beam. It can be mentioned that, as the forcing frequency approaches the value of the natural frequency of the system, the amplitude reaches the maximum value, then it starts to decrease as the forcing frequency value exceeds the natural frequency, as shown in Figure 12.

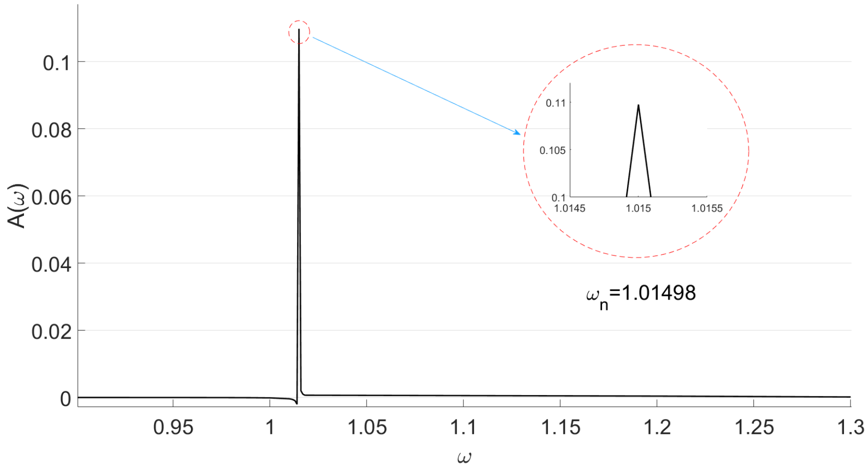


(a) First natural frequency

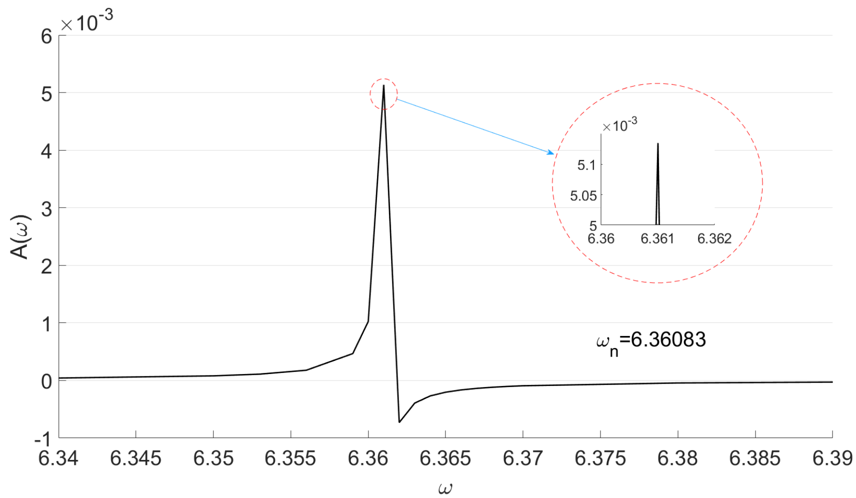


(b) Second natural frequency

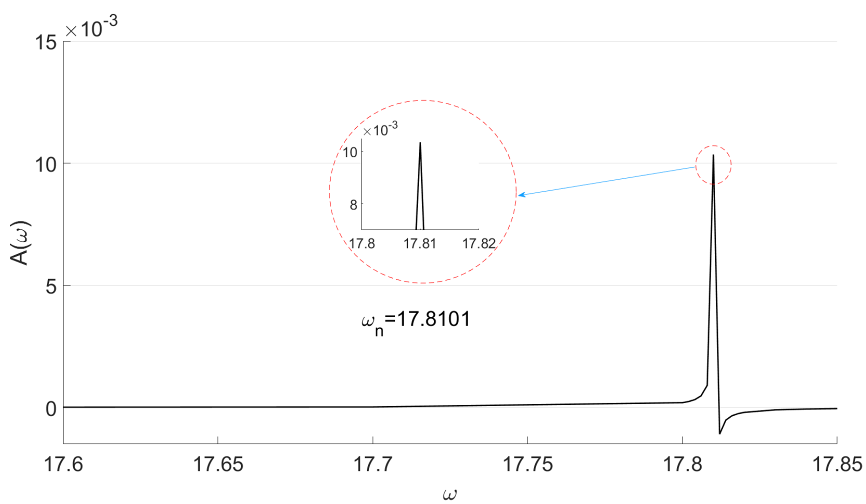


(c) Third natural frequency

Figure 12: First three natural frequencies of vibration of cantilever beam

### 4.1.7 Free Vibration of Cantilever Beam

Based on the assumption of Euler-Bernoulli beam theory, free vibration of cantilever beam was simulated using MPM. The Euler-Bernoulli beam theory was used to drive the equation of motion by performing Newton's second law of motion. The model has no external excitation applied in this analysis and, thus, the equation of motion of transverse vibration of beams is given as

$$\frac{\partial^2}{\partial x^2}\left(EI\frac{\partial^2 w}{\partial x^2}\right) + \rho A\frac{\partial^2 w}{\partial t^2} = 0 \tag{4.11}$$

The general solution of free vibration can be done by using the method of separation of variables. After mathematical analysis, the total solution of transverse vibration of the beam is found as

$$w(x,t) = \sum_{i=1}^{\infty} W_i(x)(A_i cos\omega_i t + B_i sin\omega_i t), \tag{4.12}$$

the $W_i(x)$ is the normal mode and $\omega_i$ is the natural frequency. $A_i$ and $B_i$ are constants that are determined by the initial conditions of the beam. The normal mode equation that is related to the free vibration of the beam is given as

$$W_n(x) = (cos\beta_n x + cosh\beta_n x) - \frac{cos\beta_n l + cosh\beta_n l}{sin\beta_n l + sinh\beta_n l}(sin\beta_n x - sinh\beta_n x), \tag{4.13}$$

The general natural frequency of vibration given as

$$\omega_n = (\beta_n l)^2\sqrt{\frac{EI}{\rho A l^4}} \tag{4.14}$$

For linear natural frequency, the amplitude is taken as 0.001 to ensure that the analysis is on a linear level. Figure 13 shows the mode shapes of the material point method compared with the analytical solution of the Euler-Bernoulli theory. therefore, the velocity equation that proposed in this analysis will be

$$\dot{w}(x,t) = \omega_n B_n W_n(x) cos(\omega_n, t) \tag{4.15}$$

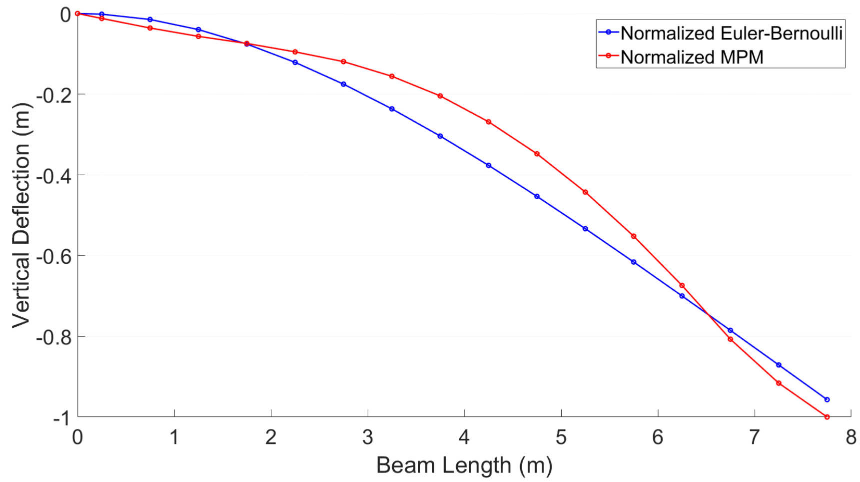


(a) First normal mode

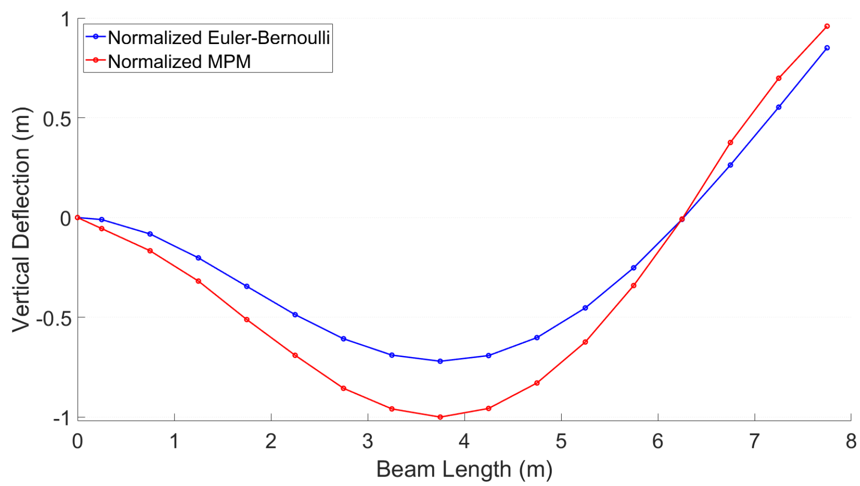


(b) Second normal mode

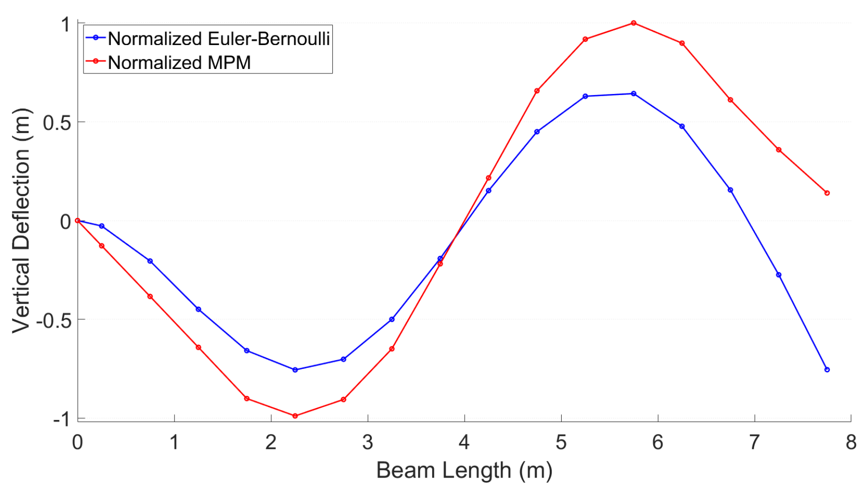


(c) Third normal mode

Figure 13: MPM normal modes compared to beam theory analysis

Table 6: First three natural frequency of cantilever beam

| Frequency | Euler-Bernoulli (Hz) | MPM (Hz) | Error |
|---|---|---|---|
| First natural frequency | 0.138 | 0.146 | 5.6% |
| Second natural frequency | 0.866 | 0.879 | 1.5% |
| Third natural frequency | 2.426 | 2.441 | 0.62% |

Where $B_n$ is a constant were assumed to equal to 1. The general natural frequency analysis was obtained from the displacement of the particles using the Fast Fourier Transform (FFT), which provides a transformation of the displacement - time domain to the frequency domain. The natural frequency of the MPM shows a slight increase when compared to Euler-Bernoulli's theory due to the large stiffness in using the linear interpolating functions. The first three natural frequencies of the analysis are given in Table 6.

#### 4.1.8 Free Vibration of Simply Supported Beam

Free vibration of the simply supported beam due to initial velocity has been studied. The mode shape of the proposed simply supported beam is given as

$$W_n(x) = C_n sin\beta_n x = C_n sin\frac{n\pi x}{l} \tag{4.16}$$

Since the beam vibrating due to initial velocity, the velocity equation is given by

$$\dot{w}(x,t) = \sum_{i=1}^{\infty} \omega_n B_n sin\frac{n\pi x}{l} cos(\omega_n t) \tag{4.17}$$

Where $B_n$ is a constant where assumed to equal to 1 in this analysis, the velocity of each point has been computed along with the period. The general natural frequency analysis was obtained from the displacement of the particles using the Fast Fourier Transform (FFT). The first three natural frequencies of the analysis are given in Table 7. Also, Figure 14 shows the normal modes related to the three natural frequencies.

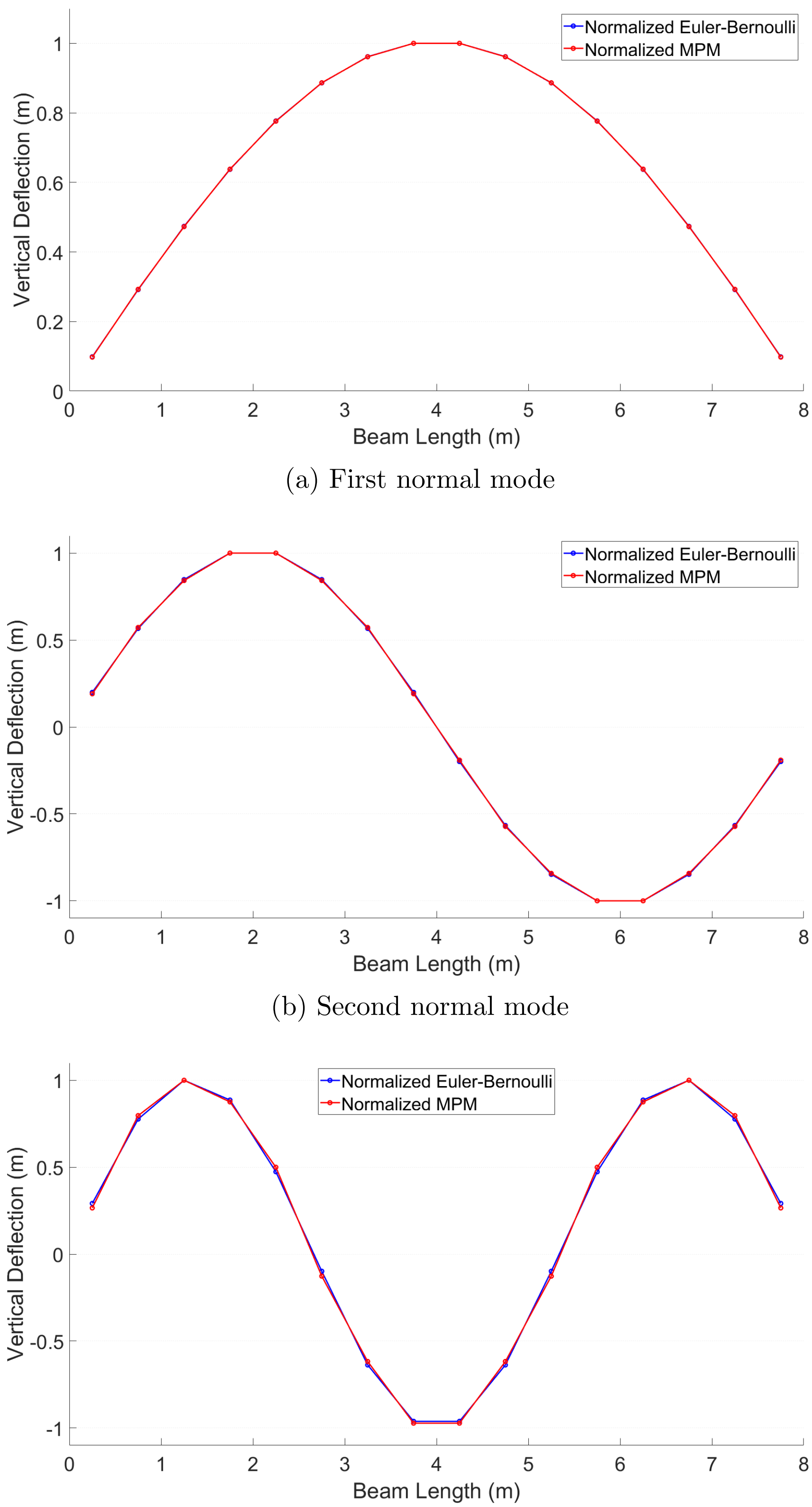

(a) First normal mode

(b) Second normal mode

(c) Third normal mode

Figure 14: MPM normal modes compared to beam theory analysis

Table 7: First three natural frequency of simply supported beam

| Frequency | Euler-Bernoulli (Hz) | MPM (Hz) | Error |
|---|---|---|---|
| First natural frequency | 0.388 | 0.391 | 0.77% |
| Second natural frequency | 1.552 | 1.563 | 0.71% |
| Third natural frequency | 3.498 | 3.516 | 0.51% |

#### 4.1.9 Free Vibration of Fixed-Fixed Beam

To show the ability of MPM in simulation beams behavior, a vibration of a fixed-fixed beam is also analyzed following the procedure discussed in previous sections. For fixed-fixed beam, the normal mode equation is as follows

$$W_n(x) = (cos\beta_n x + cosh\beta_n x) - \frac{cos\beta_n l - cosh\beta_n l}{sin\beta_n l - sinh\beta_n l}(sin\beta_n x - sinh\beta_n x), \tag{4.18}$$

and the velocity equation of fixed-fixed beam is given as,

$$\dot{w}(x,t) = \omega_n B_n W_n(x) cos(\omega_n, t) \tag{4.19}$$

The first three natural frequencies in Table 8. Also, the related normalized mode shapes are shown in Figure 15.

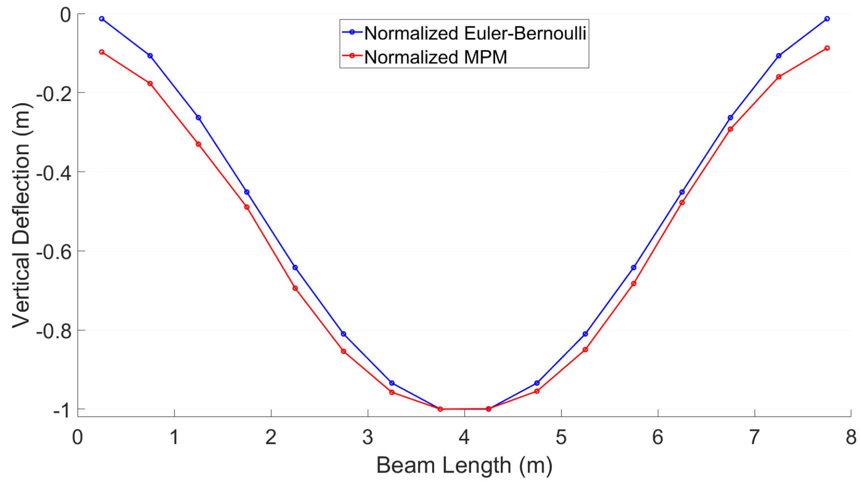


(a) First normal mode

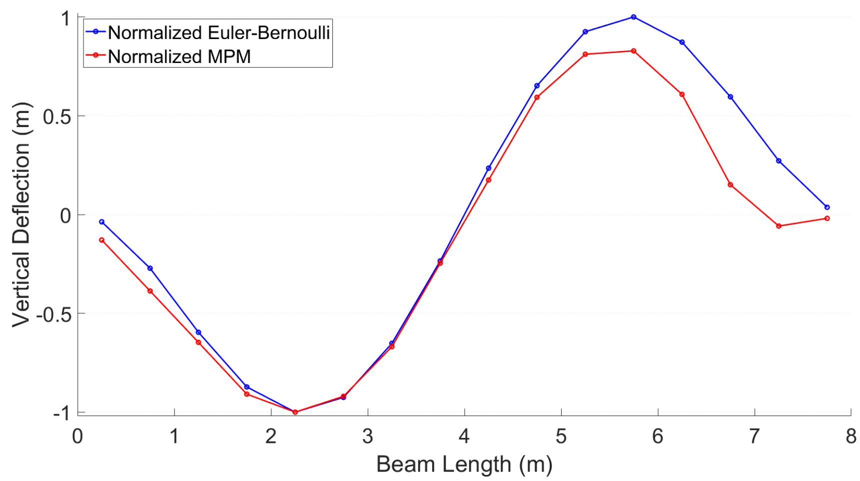


(b) Second normal mode

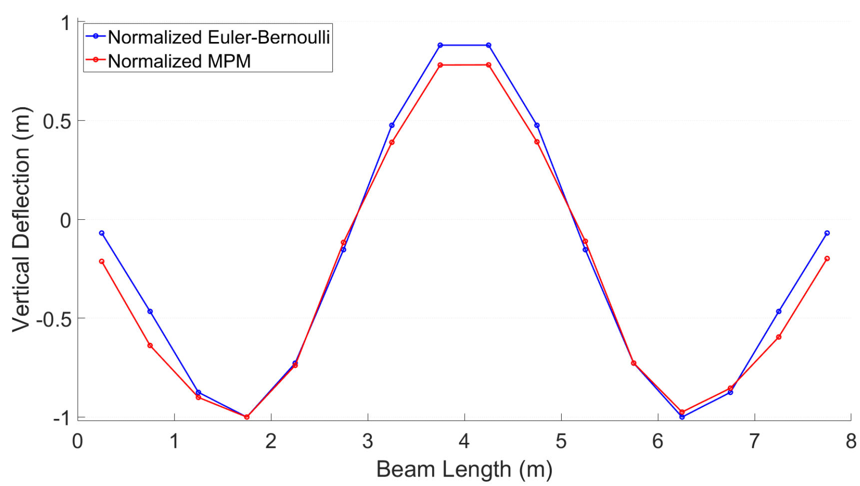


(c) Third normal mode

Figure 15: MPM normal modes compared to beam theory analysis

Table 8: First three natural frequency of fixed-fixed beam

| Frequency | Euler-Bernoulli (Hz) | MPM (Hz) | Error |
|---|---|---|---|
| First natural frequency | 0.880 | 0.879 | 0.11% |
| Second natural frequency | 2.425 | 2.441 | 0.66% |
| Third natural frequency | 4.754 | 4.736 | 0.38% |

To capture the beam response, Figure 16 provides the mode shape of the fixed-fixed beam at different time steps. It's worth mentioning that the natural frequency of the MPM shows a slight increase when compared to Euler-Bernoulli's theory due to the larger stiffness in using the linear interpolating functions for the standard material point method formulation. In addition, for both free and forced vibration beam analyses, two different procedures were used to obtain the natural frequency values. Thus, It should be mentioned that the procedure of the frequency analysis used on the forced vibration of cantilever beam analysis provides accurate outcomes in comparison to the FFT algorithm that was applied for the free vibration analysis of beams.

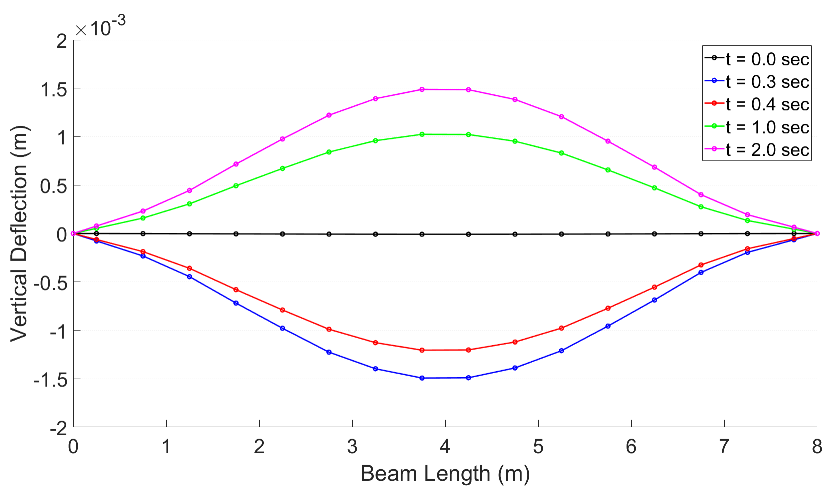


Figure 16: First mode shape at different time steps

Table 9: First three natural frequency of fixed-hinged beam

| Frequency | Euler-Bernoulli (Hz) | MPM (Hz) | Error |
|---|---|---|---|
| First natural frequency | 0.606 | 0.586 | 3.3% |
| Second natural frequency | 1.965 | 1.953 | 0.61% |
| Third natural frequency | 4.099 | 4.102 | 0.07% |

#### 4.1.10 Free Vibration of Fixed-Hinged Beam

Following the assumption made for the cantilever beam vibration, fixed-hinged beam vibration has been examined using MPM. The first three natural frequencies are shown in Table 9 while the mode shapes are plotted in Figure 17.

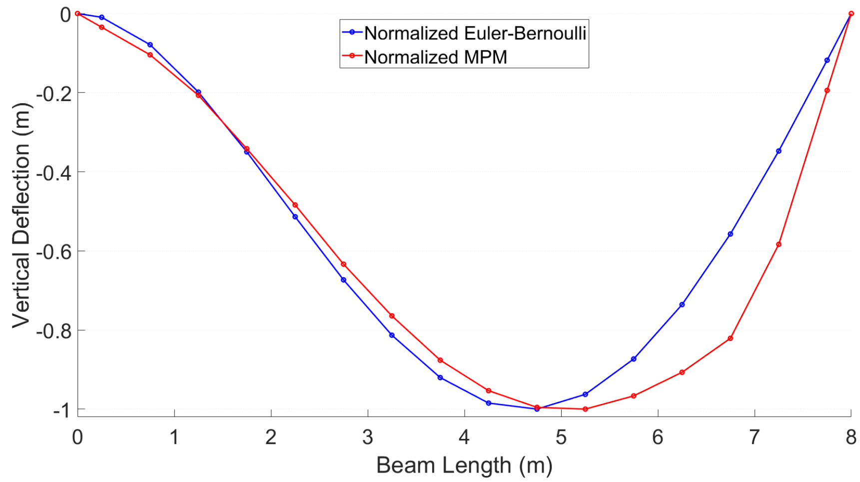


(a) First normal mode

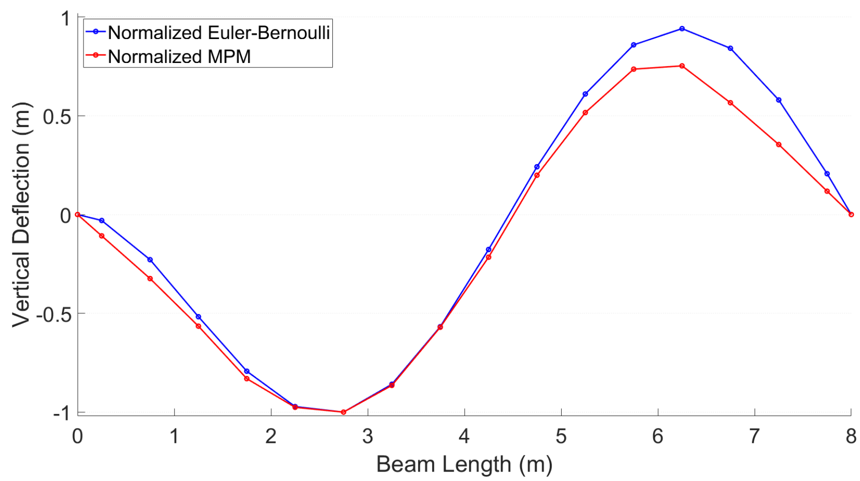


(b) Second normal mode

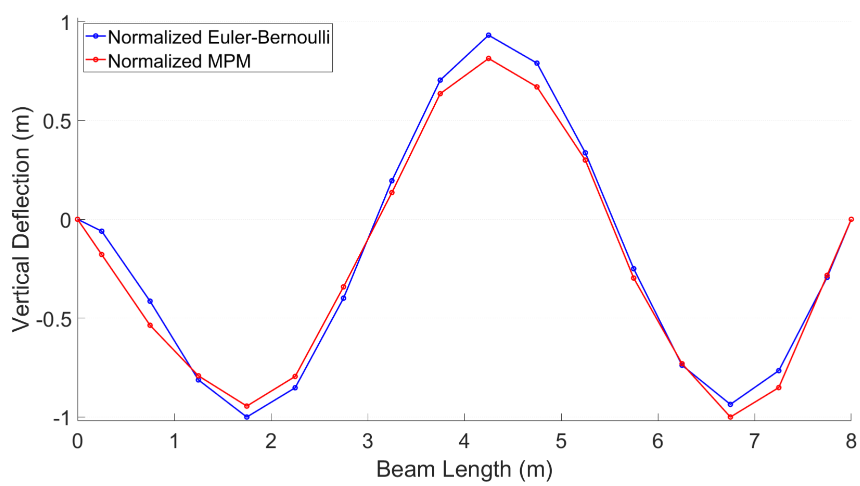


(c) Third normal mode

Figure 17: MPM normal modes compared to beam theory analysis

## 4.2 Large Deformation of Beams Mechanics

### 4.2.1 Introduction

For the nonlinear vibration analysis, the deformation is assumed to be moderately large to ensure the stability of the dynamic frame of the explicit MPM formulation. In addition, the analysis of the first natural frequency is related to the fundamental mode shape. All beams model were selected with height $h = 1\ m$, and the modulus of elasticity $E = 3000\ Gpa$ with different lengths. The linear natural frequency is computed following the Euler-Bernoulli theory as

$$\omega_n = (\beta_n l)^2 \sqrt{\frac{EI}{\rho A l^4}} \tag{1}$$

Beams were discretized to 72 elements with 64 embedded material points over the beam domain. The nonlinear frequencies are computed for several $a/r$ values, where $a$ is the amplitude and the $r$ is the radius of gyration. The amplitude was taken at the mid-span of the beam. The linear frequency was computed following the assumption of the Euler-Bernoulli theory.

### 4.2.2 Nonlinear free vibration of Simply Supported Beam

Moderately large deformation is assumed to be the governed assumption in this problem, where the stretching of the natural axis generates axial displacement that affects the value of the natural frequency. Here, the nonlinear frequencies were obtained using the material point method for the simply supported beam at the particle close to the mid span. The boundary conditions were also applied to the nodal momentum and the resultant force functions. The frequencies are expressed in terms of $(\omega_{NL}/\omega_L)^2$ . Table 10 shows the obtained values of $(\omega_{NL}/\omega_L)^2$ for the $L/r = 27.713$.

The nonlinear natural frequencies were computed using the Fast Fourier transform (FFT) for each $a/r$ value. Figure 18 shows the nonlinear frequencies obtained using FFT theory

Table 10: $(\omega_{NL}/\omega_L)^2$ ratio for simply supported beam

| | $L/r = 13.856$ | $L/r = 27.713$ | KRIEGER [63] |
|---|---|---|---|
| a/r | $(\omega_{NL}/\omega_L)^2$ | $(\omega_{NL}/\omega_L)^2$ | $(\omega_{NL}/\omega_L)^2$ |
| 0.1 | 1.0071 | 1.0023 | 1.0025 |
| 0.2 | 1.0103 | 1.0095 | 1.0100 |
| 0.4 | 1.0485 | 1.0468 | 1.0400 |
| 0.6 | 1.0922 | 1.0907 | 1.0900 |
| 0.8 | 1.1769 | 1.1569 | 1.1600 |
| 1.0 | 1.2626 | 1.2402 | 1.2500 |

for the first three $a/r$ values.

### 4.2.3 Nonlinear free vibration of Fixed - Fixed Beam

To capture the lowest bending mode behavior, the boundary conditions are applied to the related nodes in terms of nodal momentum and resultant force functions. In this case, the initial velocity is the same as those used for the case of the linear fixed-fixed vibration. However, the focus is now on the amplitude influence associated with the lowest bending mode.

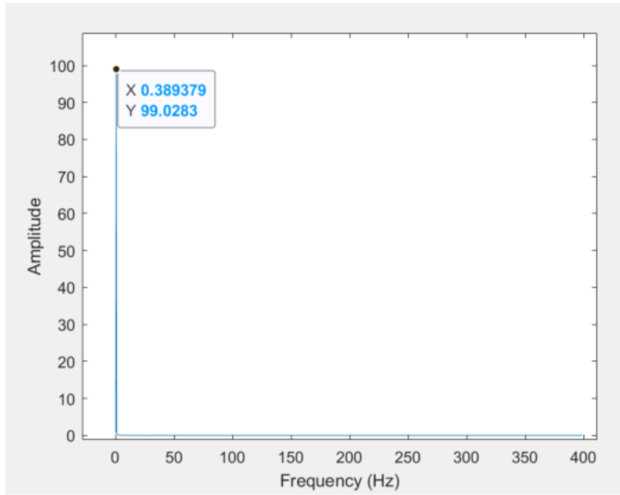


(a) a/r =0.1

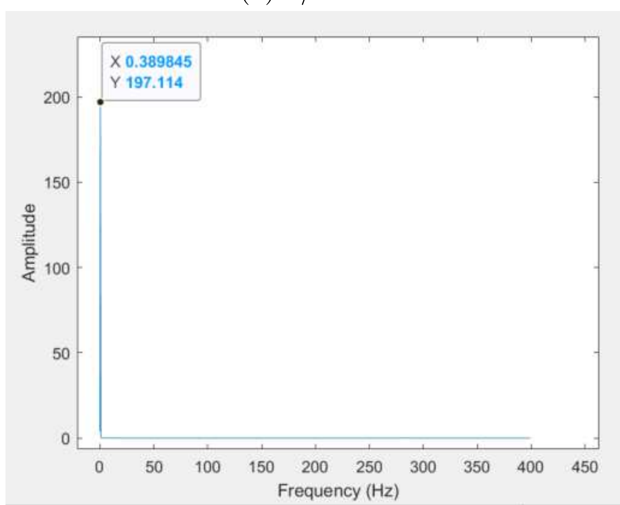


(b) a/r =0.2

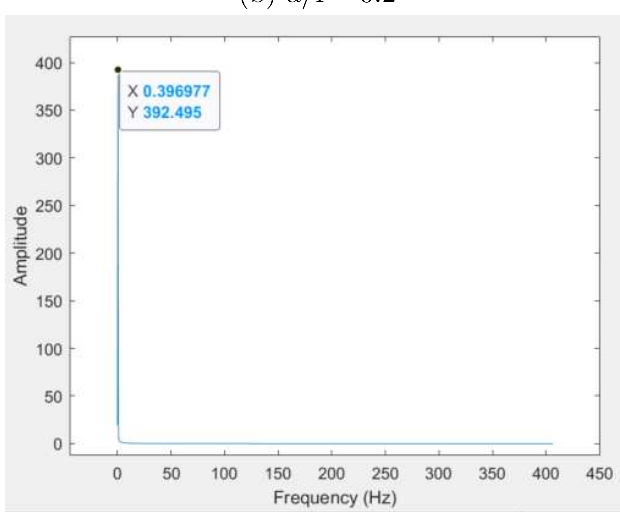


(c) a/r =0.4

Figure 18: Nonlinear frequencies for simply supported beam when $L/r = 27.713$

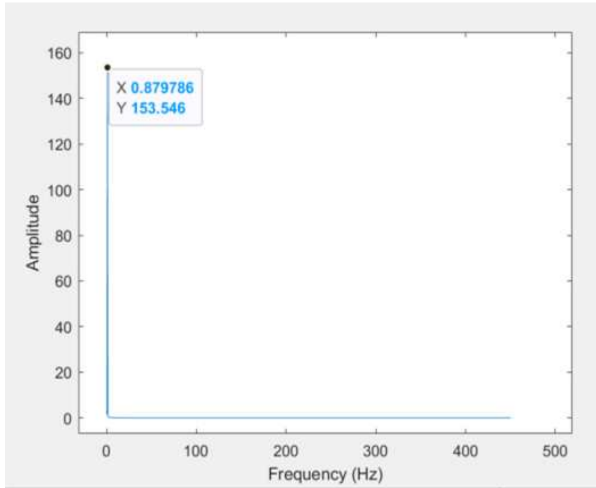


(a) a/r =0.1

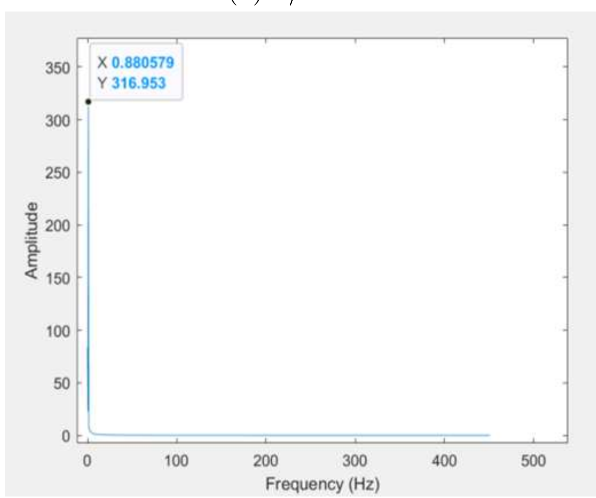


(b) a/r =0.2

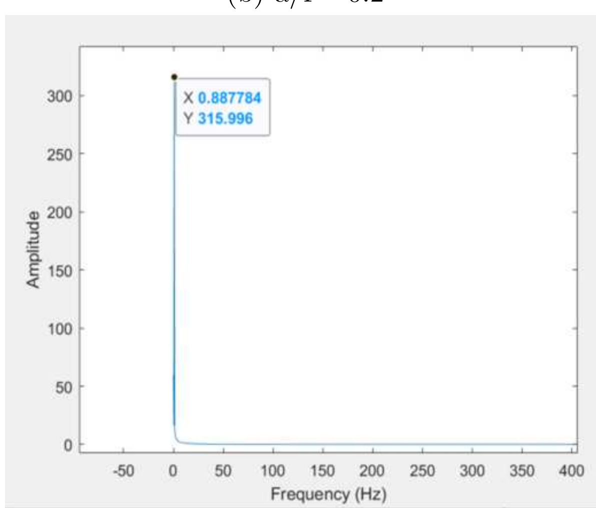


(c) a/r =0.4

Figure 19: Nonlinear frequencies for Fixed-Fixed beam when $L/r = 27.713$

Table 11: $(\omega_{NL}/\omega_L)^2$ ratio for Fixed-Fixed beam

| | $L/r = 13.856$ | $L/r = 27.713$ | EVENSON [15] |
|---|---|---|---|
| a/r | $(\omega_{NL}/\omega_L)^2$ | $(\omega_{NL}/\omega_L)^2$ | $(\omega_{NL}/\omega_L)^2$ |
| 0.1 | 1.0002 | 1.0002 | 1.0006 |
| 0.2 | 1.0039 | 1.0020 | 1.0024 |
| 0.4 | 1.0204 | 1.0185 | 1.0096 |
| 0.6 | 1.0373 | 1.0277 | 1.0216 |
| 0.8 | 1.0566 | 1.0372 | 1.0384 |
| 1.0 | 1.0968 | 1.0605 | 1.0599 |

#### 4.2.4 Nonlinear free vibration of Fixed - Hinged Beam

In the case of the fixed-hinge beam, the system should also include the increased amplitude's effect on the frequency response. Fundamental mode shape was captured and explained in the linear vibration sections; however, the boundary condition in this example was applied to the nodal velocity functions along with the resultant force functions to examine the ability of MPM to simulate the beam behavior. Table 12 shows the nonlinear frequency ratio for different $a/r$ values. Also, the Figure 20 describes the FFT analysis for the first three $a/r$ values.

#### 4.2.5 Total Lagrangian Material Point Method

A recent TLMPM study was done by de Vaucorbeil et al. [9] for the vibration of a compliant bar subjected to the gravity field. The objective was to examine the TLMPM stability by extension the work of Sadefhirad et al. [28] by modeling the 2D TLMPM. The generated displacement of the tracked material point presents a stable harmonic behavior through the time simulation. Further, the model extended to 3D; forming a uniform cube with the same material properties used in the 2D model. Shape functions of standard MPM have been

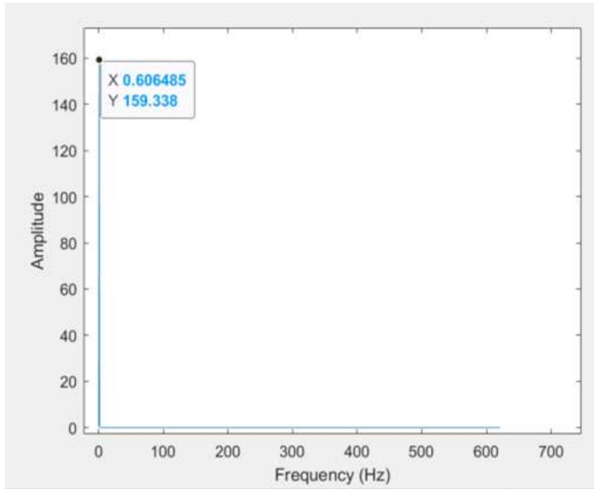


(a) a/r =0.1

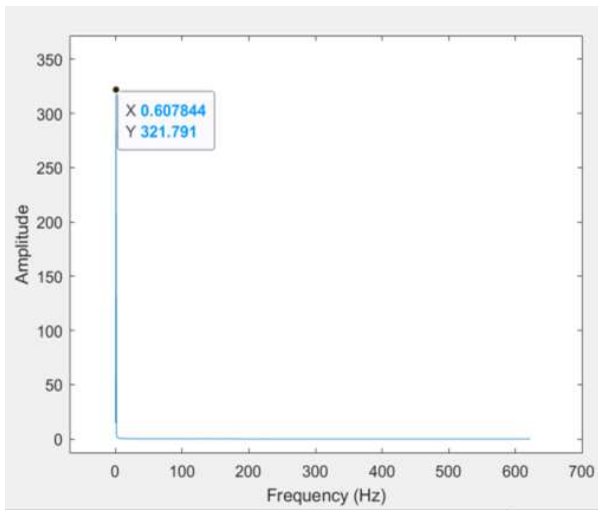


(b) a/r =0.2

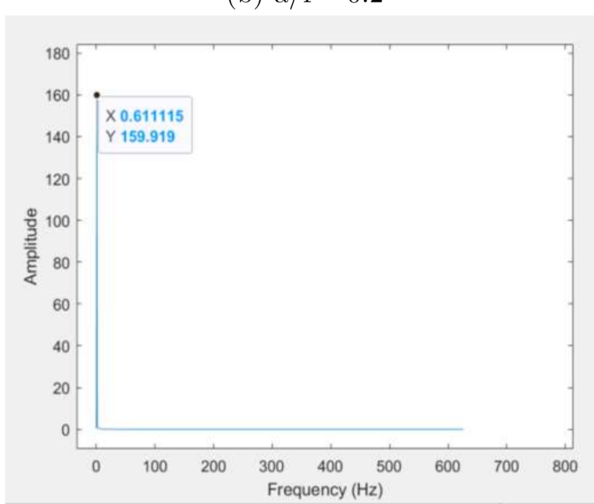


(c) a/r =0.4

Figure 20: Nonlinear frequencies for Fixed- Hinged beam when $L/r = 27.713$

Table 12: $(\omega_{NL}/\omega_L)^2$ ratio for Fixed-Hinged beam

| | $L/r = 13.856$ | $L/r = 27.713$ | KRIEGER [63] | EVENSON [15] |
|---|---|---|---|---|
| a/r | $(\omega_{NL}/\omega_L)^2$ | $(\omega_{NL}/\omega_L)^2$ | $(\omega_{NL}/\omega_L)^2$ | $(\omega_{NL}/\omega_L)^2$ |
| 0.1 | 1.0035 | 1.0007 | 1.0013 | 1.0013 |
| 0.2 | 1.0060 | 1.0053 | 1.0053 | 1.0053 |
| 0.4 | 1.0136 | 1.0162 | 1.0213 | 1.0214 |
| 0.6 | 1.0608 | 1.0637 | 1.0479 | 1.0481 |
| 0.8 | 1.0856 | 1.0887 | 1.0850 | 1.0854 |
| 1.0 | 1.1380 | 1.1413 | 1.1323 | 1.1335 |

adopted this time to study the qualitative of the TLMPM formulation. Although various assumptions are adopted in this model, the TLMPM still performs stability and does not generate any numerical fracture. At the same time, the result generally was in satisfactory agreement with the finite element model used in that examination.

According to this study, the Total-Lagrangian material point method presents stable behavior for solids undergoing large deformation as well as refined material point method formulation under extreme applied load. Further, TLMPM shows considerable efficiency comparing to the various material point method formulations. To warm up, the TLMPM could be adopted to examine solid behaviors with various geometries assumptions. To validate the formulation of the TLMPM analysis the bar vibration due to gravity load that [9] simulated was replicated and the results are shown in Figure 21.

Also, for the small deformation assumption, the free vibration of the bar has been simulated using the TLMPM. The bar geometries and assumptions as the same as the ULMPM introduced in section 4.1.3. The result compared with the exact solution as shown in Figure 22, where the simulated result created excellent agreement behavior with an analytical solution. A cantilever beam subjected to uniformly distributed load was studied for a static beam under moderated large deformation. Heyliger and Reddy [22] completed this analysis . As shown in Figure 23, The result shows that the TLMPM under moderated large deformation

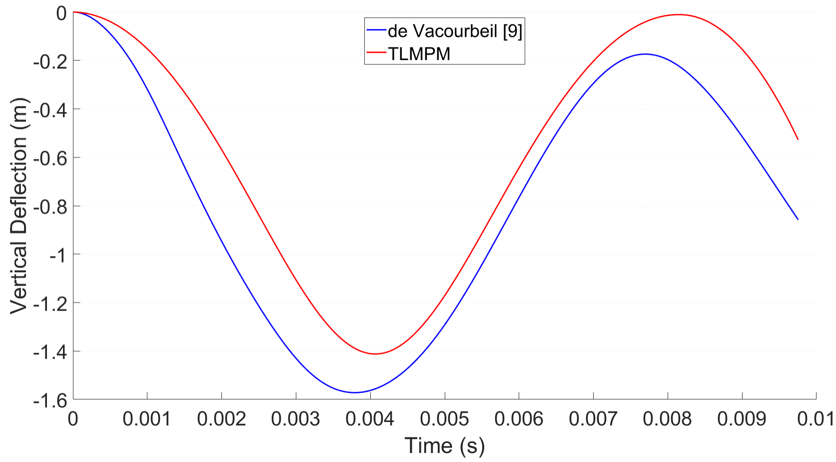


Figure 21: Vertical bar vibration under gravity load

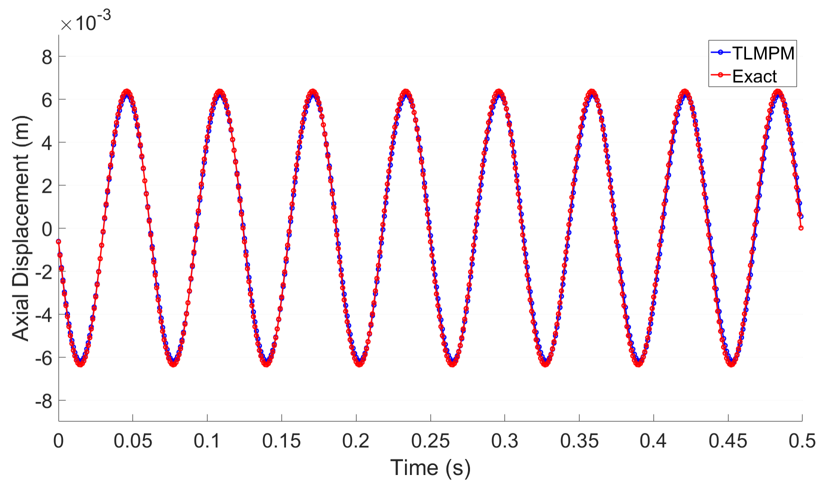


Figure 22: Free vibration of bar using TLMPM

generates a behavior for the stiffening beam in agreement with the elasticity solution done in [22]. In addition, as the load increases, the TLMPM provides larger displacement compared to the FEM analysis due to the ability of TLMPM to handle large deformation analysis better than FEM.

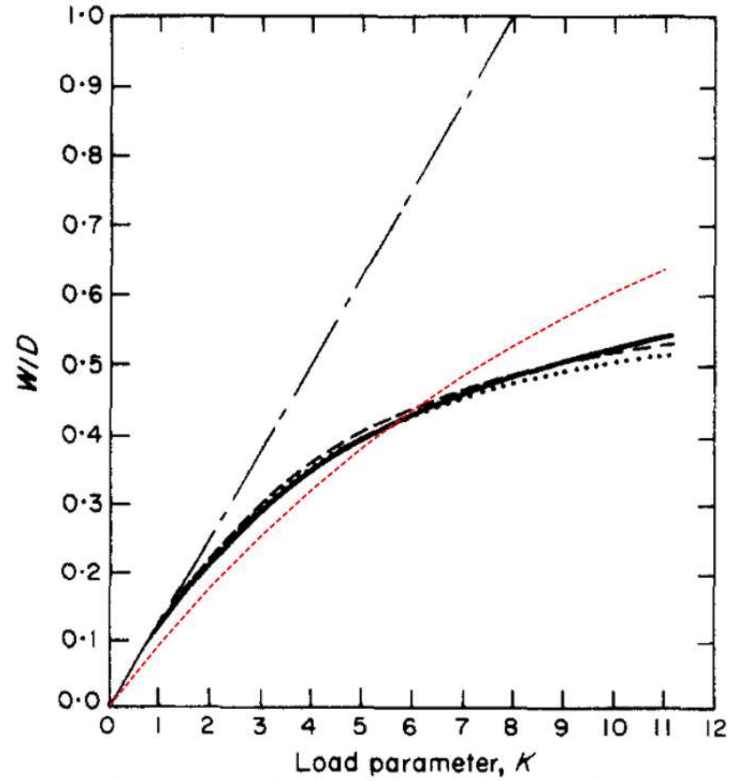


Figure 23: Cantilever beam results (red dashed line) compared to Heyliger and Reddy results [22]

# 5 DAMAGE MECHANICS USING MATERIAL POINT METHOD

Damage of materials has been examined based on different damage models that reflect the characteristic variations of material properties and failure processes. The damage variable can be obtained by microstructural analysis or by experimental test analysis. Different damage variables can be used based on the different phenomena of materials. For instance, the effective stress concept was adopted for Kachanov [27] Lemaitre and Chaboche [29] and Westlund [51] to define the damage variable while Rosuselier [52] included the mass density of the failed material.

Structures failure can be modeled using the Material Point Method. Considering damage analysis, MPM could be adopted to study the effects of loaded structures for different assumptions. The slab bridge can be modeled as a thin plate as done by [42] which provided a simple beam-plate model using the finite element method. Also, Minalu[37] assumed the bridge deck to be an orthotropic plate model. The beam and slab type bridge was converted to an equivalent slab system. The finite element model was created using SCIA Engineer. Also, slab bridge loaded until the failure has been studied by researchers of University of Cincinnati and Delft University of Technology using nonlinear finite element model[54]. The slab of the bridge is modeled as a shell/ plate element with different assumptions of beam-columns or supports. Large deformation of failure analysis of slope examined using smoothed particle finite element method[36].

In order to enhance the safe design, computational analysis requires a proper evaluation of structure subjected to different load conditions. An appropriate selection of the constitutive relations is challenging due to the need for an accurate description of material behavior under different conditions. It's known that the permanent changes in structure are related to the nonlinear response of the material; therefore, the formulation of constitutive equations should include the mechanical concepts related to these changes that might be as a slip or micro-cracking.

## 5.1 Damage Constitutive Model

In rock mechanics, the constitutive model is crucial in developing numerical analysis. A rock structure is supposed to be composed of numerous mesoscopic elements, which allow including micro cracks. In addition, these mesoscopic elements are small enough to be treated as particles that should be analyzed using continuum mechanics. The constitutive model of elastic isotropic rock materials in uniaxial experiments is given as

$$\sigma_1 = E\epsilon_1 \tag{5.1}$$

where $\sigma_1$ is the axial stress, E is the modulus of elasticity of the rock material, and $\epsilon_1$ is the axial strain. For damaged rock materials, the constitutive model becomes

$$\sigma_1 = E(1 - D)\epsilon_1 \tag{5.2}$$

D here is the damage variable that is a measure for material degradation. Including the damage variable in the constitutive equation lead the impact of micro cracks to be included in the response of the rock. This equation is known as the rock damage constitutive model. In MPM, it is known that the stress of the current time step is obtained using the updated stress increment from the strain updating. Hence, the rock damage constitutive equation in MPM form is as follows

$$\sigma_p^n = \sigma_p^{n-1} + E_p(1 - D)\epsilon_p^n \tag{5.3}$$

where $E_p$ is the modulus of elasticity of the material point and $\epsilon_p^n$ is the updated strain of the material point.

The distribution of rock stress function was assumed to be empirical Weibull distribution [11]. According to the Weibull failure criterion, the Weibull distribution work conjugate with the ultimate material strength. The probability density function of the Weibull random variable is

$$f(x; \lambda, m) = \begin{cases} \frac{m}{\lambda}\left(\frac{x}{\lambda}\right)^{m-1} \quad \exp\left\{-\left(\frac{x}{\lambda}\right)^m\right\}, x, & x > 0 \\ 0, & x \leq 0 \end{cases} \tag{5.4}$$

where $m > 0$ is the shape parameter and $\lambda > 0$ is the scale parameter of the distribution. The cumulative distribution function for the Weibull distribution is

$$F(x; \lambda, m) = \begin{cases} 1 - \exp\left\{-\left(\frac{x}{\lambda}\right)^m\right\}, x, & x > 0 \\ 0, & x \leq 0 \end{cases} \tag{5.5}$$

So, the rock analysis uses the material point method. the survival probability $P_s(V_{ref})$ of a material point subjected to maximum stress $\sigma$ computed as

$$P_s(V_{ref}) = \exp\left\{ -\left(\frac{\sigma}{[\sigma]}\right)^m \right\} \tag{5.6}$$

Where $[\sigma]$ is the reference stress that can be assumed as a kind of reference strength parameter. Based on Weibull's theory, the survival probability from tensile damage P(st) of the material point under maximum principal stress can be obtained as

$$P_{st} = \exp\left[ -\left(\frac{\sigma}{f_t}\right)^m \right] \tag{5.7}$$

where$f_t$ is the mean uniaxial tensile strength, $m$ is the shape parameter that reflects how the probability would reduce as $\sigma$ hits the strength $f_t$. In this study, the compression strength of the rock is applied to (5.2) in order to simulate the compression analysis of Trajan's column. Therefore, the equation (5.7) will be

$$P_{st} = \exp\left[ -\left(\frac{\sigma_c}{f_c}\right)^m \right] \tag{5.8}$$

According to [11], the rock damage variable for Weibull theory is expressed as

$$D = 1 - \exp\left[ -\left(\frac{\sigma_c}{f_c}\right)^m \right] \tag{5.9}$$

Thereby, the Weibull distribution damage constitutive law or Weibull model for the uniaxial compression analysis becomes

$$\sigma_1 = E\exp\left[ -\left(\frac{\sigma_c}{f_c}\right)^m \right]\epsilon_1 \tag{5.10}$$

By substituting (5.10) to (5.2), the damaged constitutive equations of rocks in the material point method scheme are computed as

$$\sigma_p^n = \sigma_p^{n-1} + E_p\left\{ \exp\left[ -\left(\frac{\sigma_c}{f_c}\right)^m \right] \right\}\epsilon_p^n \tag{5.10}$$

The following section will describe the analysis made on real life model using the proposed formulations with different material assumptions.

# 6 AXISYMMETRIC SOLID

To allow the 3D solid behavior to be inherent to a 2D model, axisymmetric solids formulation takes place, especially with solids with axial symmetry. Thus, the solids geometrical and material characteristics become independent of the circumferential coordinate $\theta$ as shown in Figure 24. In these solid assumptions, the load is also axisymmetric where the displacement vector has only two components in the radial and axial axial axes. Axisymmetric solids can be represented in different engineering structures such as; water and oil tanks, cooling towers, domes and cylindrical structures, as shown in Figure 25.

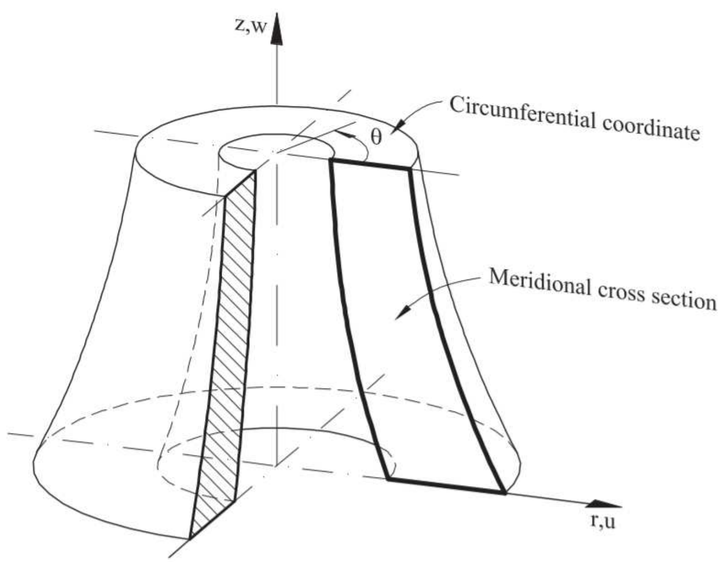


Figure 24: Axisymmetric solid

## 6.1 Basic Formulation

### 6.1.1 Displacement field

Consider the axisymmetric solid subjected to the axisymmetric loading shown in Figure 24. The radial movement of any point is identified as $(u)$ while the axial displacement of this point is represented by $(w)$. The circumferential displacement$(v)$ is assumed to be zero

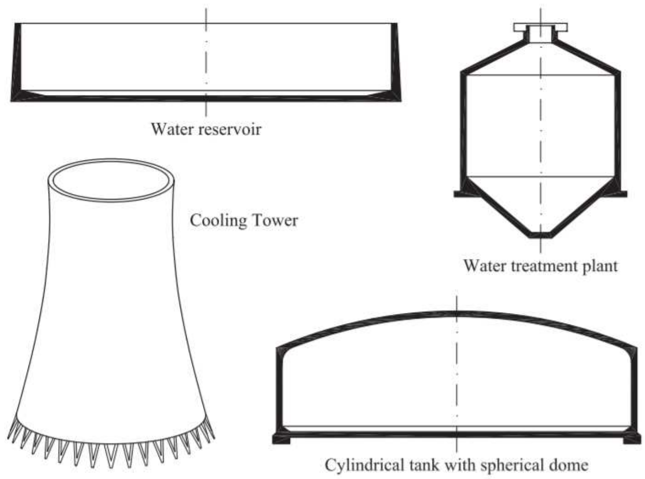


Figure 25: Some axisymmetric structures

because of the axial symmetry. Thereby, the displacement vector is given as

$$\mathbf{u} = \begin{Bmatrix} u(r,z) \\ w(r,z) \end{Bmatrix} \tag{6.1}$$

### 6.1.2 Strain field

Because the solid is assumed to be axial symmetry in this formulation, the displacement vectors $u$ and $w$ are independent of the circumferential coordinate $\theta$. As a result, the shear strains $\gamma_{r\theta}$ and $\gamma_{z\theta}$ are zero. Therefore, the strains field are given as

$$\epsilon_r = \frac{\partial u}{\partial r} \quad ; \quad \epsilon_r = \frac{\partial w}{\partial z} \quad ; \quad \gamma_{rz} = \frac{\partial u}{\partial z} + \frac{\partial w}{\partial r} \tag{6.2}$$

where $\epsilon_r$ , $\epsilon_z$ and $\gamma_{rz}$ are the radial, axial and tangential strains, respectively.
The circumferential strain generated due to the axial deformation, this strain measure can be computed as

$$\epsilon_\theta = \frac{2\pi(r+u) - 2\pi r}{2\pi r} = \frac{u}{r} \tag{6.3}$$

in which explains the movement of the point from the circumference of radius $r$ to a circumference of radius $r + u$. Therefore, the strain vector of any point includes four components as

$$\epsilon = \begin{bmatrix} \epsilon_r, & \epsilon_z, & \epsilon_\theta, & \gamma_{rz} \end{bmatrix}^T = \begin{bmatrix} \frac{\partial u}{\partial r}, & \frac{\partial w}{\partial z}, & \frac{u}{r}, & \frac{\partial u}{\partial z} + \frac{\partial w}{\partial r} \end{bmatrix}^T \tag{6.4}$$

### 6.1.3 Stress field

The stress are related to strain measures as follow

$$\epsilon = \begin{bmatrix} \sigma_r, & \sigma_z, & \sigma_\theta, & \tau_{rz} \end{bmatrix}^T \tag{6.5}$$

here $\sigma_r$, $\sigma_z$ and $\sigma_\theta$ are, respectively, the radial, axial and circumferential stresses and $\tau_{rz}$ is the tangential stress while the other stresses are zero. The sign convention for all stresses is shown in Figure 26.

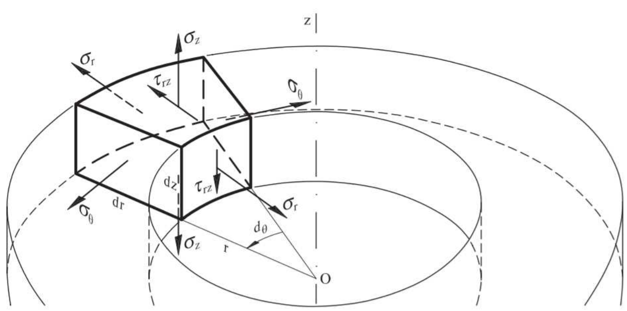


Figure 26: Stresses acting on a differential volume of an axisymmetric solid underaxisymmetric loading

### 6.1.4 Constitutive equation

The relationship between stress and strain in axisymmetric solid as

$$\sigma = \mathbf{D}(\epsilon - \epsilon^0) + \sigma^0 \tag{6.6}$$

This equation includes the initial stains $\epsilon^0$ and stresses $\sigma^0$ components. Matrix $\mathbf{D}$ for the isotropic material can be computed as

$$\mathbf{D} = \frac{E}{(1+\nu)(1-2\nu)} \begin{bmatrix} 1-\nu & \nu & 0 & 0 \\ \nu & 1-\nu & 0 & 0 \\ 0 & 0 & 1-\nu & 0 \\ 0 & 0 & 0 & \frac{1-2\nu}{2} \end{bmatrix} \tag{6.7}$$

In this study, the thermal isotropic case is not included; therefore, both the initial stains $\epsilon^0$ and initial stresses $\sigma^0$ components are going to be neglected in (6.6).

## 6.2 Trajan's Column

Ancient structures are always unique and represent people's historical, cultural and emotional values. Because of these, they consider precious structures that could associate with the effects on different aspects of any society. Some countries and entities consider many historical assets as attractions that would reflect positively on the economy. In addition, They could explain significant events that affected the country's history. Protection of such structures is critical and challenging due to various parameters like size, the age of the used material, and the construction condition at that time. Studying their ability to withstand is an essential aspect of tracking the workability and the safety of such structures.

Trajan's column is one of the ancient structures in Rome, Italy. The column constructions were completed in AD 113 under the supervision of the architect Apollodorus. It represents the Roman emperor Trajan's victory against the Dacian wars. It has 98 feet in height and is formed by 20 drums of marble; each drum weighs 32 tons.

The failure test is done to the whole column's shape during compression loading using MPM. Due to the cylindrical geometry of the column, the axisymmetric model was adopted in the analysis with materials properties that are independent of the circumferential coordinate $\theta$. The column modeled with height $h = 43\ m$, width $w = 1.85\ m$. Based on experimental data, the modulus of elasticity of marble is 22.2 $Gpa$ while the density of marble $\rho = 2711\ kg/m^3$. The column was discretized to 430 elements with initial 172 material points.

Figure 27: Trajan's column

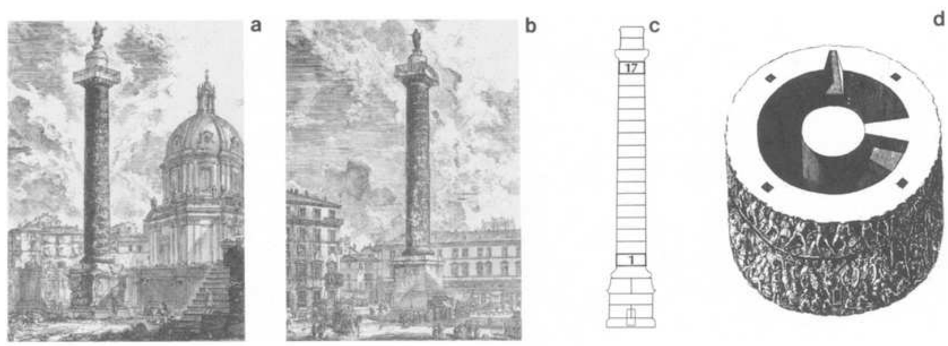


Figure 28: Trajan's cloumn drums distrubution

The test was conducted by applying an axial load at a constant rate with respect to time until the maximum principal stress hits the compression strength of the marble. Based on Anastasiadis et al. [2], the typical marble stress-strain curve can be divided into three different behaviors, as shown in Figure 29. In the first behavior, a nonlinear response between stress and strain relationship appears due to the closing of pores under the applied load impact. This behavior is very short and referred to as the quasi- plastic range, and it does not extend 0.1 of maximum stress. Then, along linear behavior between stress and strain appears, which corresponds to the linear elastic response of rocks. After that, the plastic behavior starts and the linearity does not appear anymore, and the plastic response continues up to fracture. It is worth mentioning that the material point simulation behaves as a typical marble stress-strain curve considering the three different behavior shown in Figure 29.

The macroscale simulation of uniaxial compression of the column was compared with a laboratory test of marble done by Mahmutoglu [34]. The stress was applied by a loading function with a constant rate $1 \times 10^{-3}$ sec for every point along the column. The results agree with experimental data, especially when the material point number increased, in which both failure stress and strain of the column converge to the test values, as shown in Figure 30.

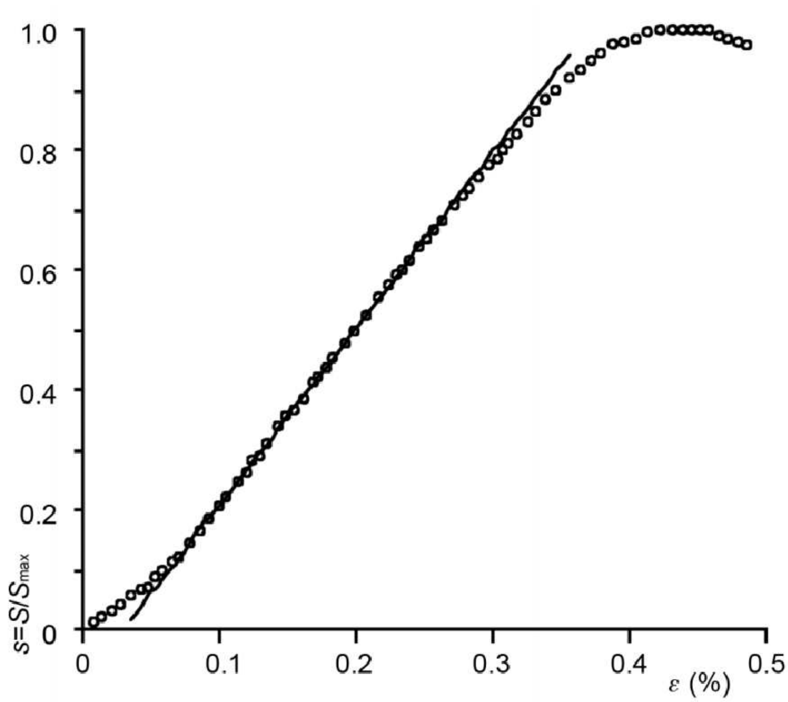


Figure 29: Typical marble stress-strain curve by Anastasiadis et al [2]

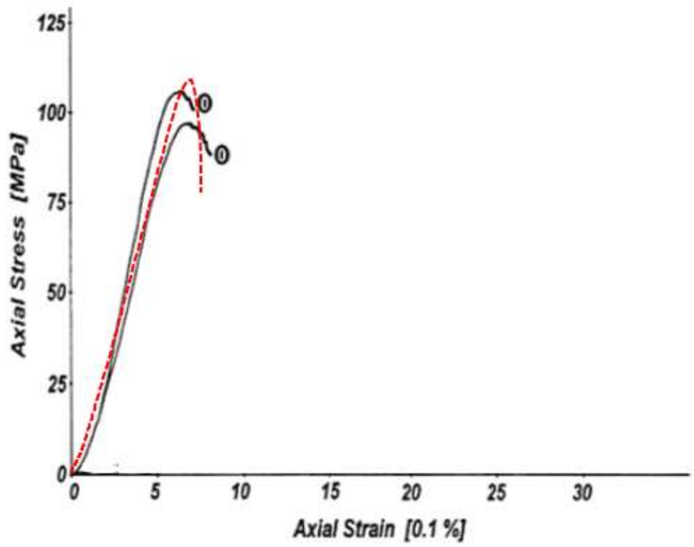


(a) 172 points

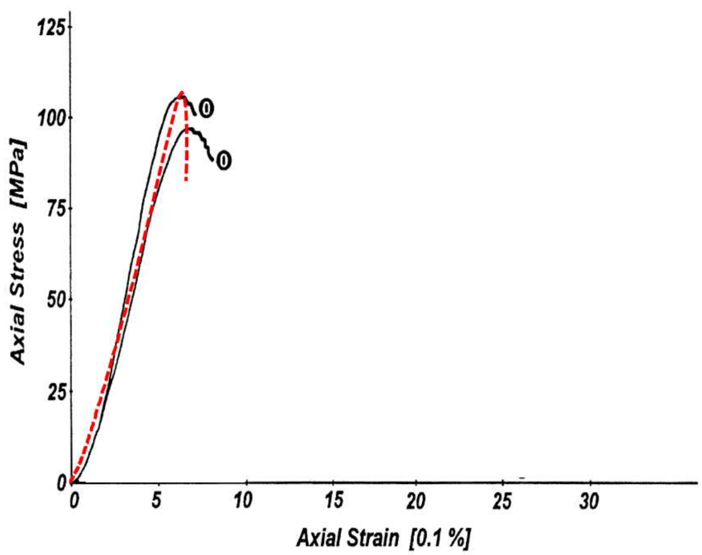


(b) 688 points

Figure 30: Stress- strain curve of Trajan's column (Red dashed lines) compared with laboratory test of Carrara marble of Mahmutoglu [34]

## 6.3 Phyllostachys Edulis bamboo

Phyllostachys edulis bamboo is also known as Moso bamboo, considered the most crucial bamboo type in China and Taiwan. It is one of the giant bamboo species in the world by height, reaches 92 ft and is used widely in wood textile manufactory. Bamboo generally provides good mechanical features such as elasticity and toughness along with the excellent environmental influence of low carbon energy-saving properties that make it one of the adopted construction components in different applications. In this study, the compression test will be simulated using MPM to study the proposed constitutive relation for such material and bamboo responses of the model with [30].

Figure 31: Phyllostachys Edulis bamboo

The bamboo scrimber was adopted for the compression test using MPM. Based on the experimental conditions of bamboo scrimber, the tested samples were dried under a temperature reached 165. Therefore, the model is assumed to be a drained bamboo scrimber. The general damage constitutive model was adopted in the constitutive relation. The load is applied incrementally with a small load rate and the mechanical properties are extracted from the

Table 13: Mechanical properties of the Phyllostachys edulis bamboo

| $E_1(GPa)$ | $E_2(GPa)$ | $\nu$ |
|---|---|---|
| 4.31 | 14.16 | 0.38 |

experimental stress-strain curve described in Table [13]. The model is discretized to an orthotropic strip, as shown in Figure 32.

In the simulation, the sample's mechanical properties were adopted from the experimental results based on the mean values of elastic modulus, ultimate stress and Poisson's ratio. The simulated stress-strain curves show good coincided agreement to the experiment and theoretical results introduced by Li et al. [30]; however, the ultimate strength of the MPM model shows a smaller peak stress value in compression to the experiments. Generally, the material point method simulation can express the brittle damage features of the Phyllostachys edulis bamboo specimens in satisfactory agreement with the experiment, as shown in Figure 33.

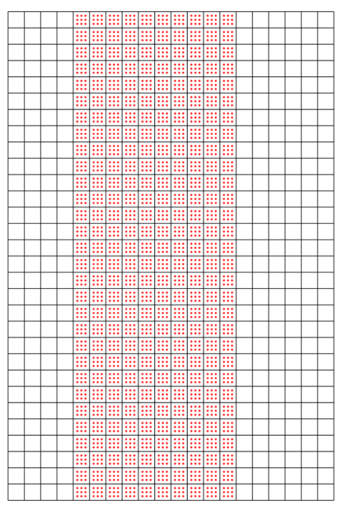

Figure 32: MPM mesh of Phyllostachys Edulis bamboo

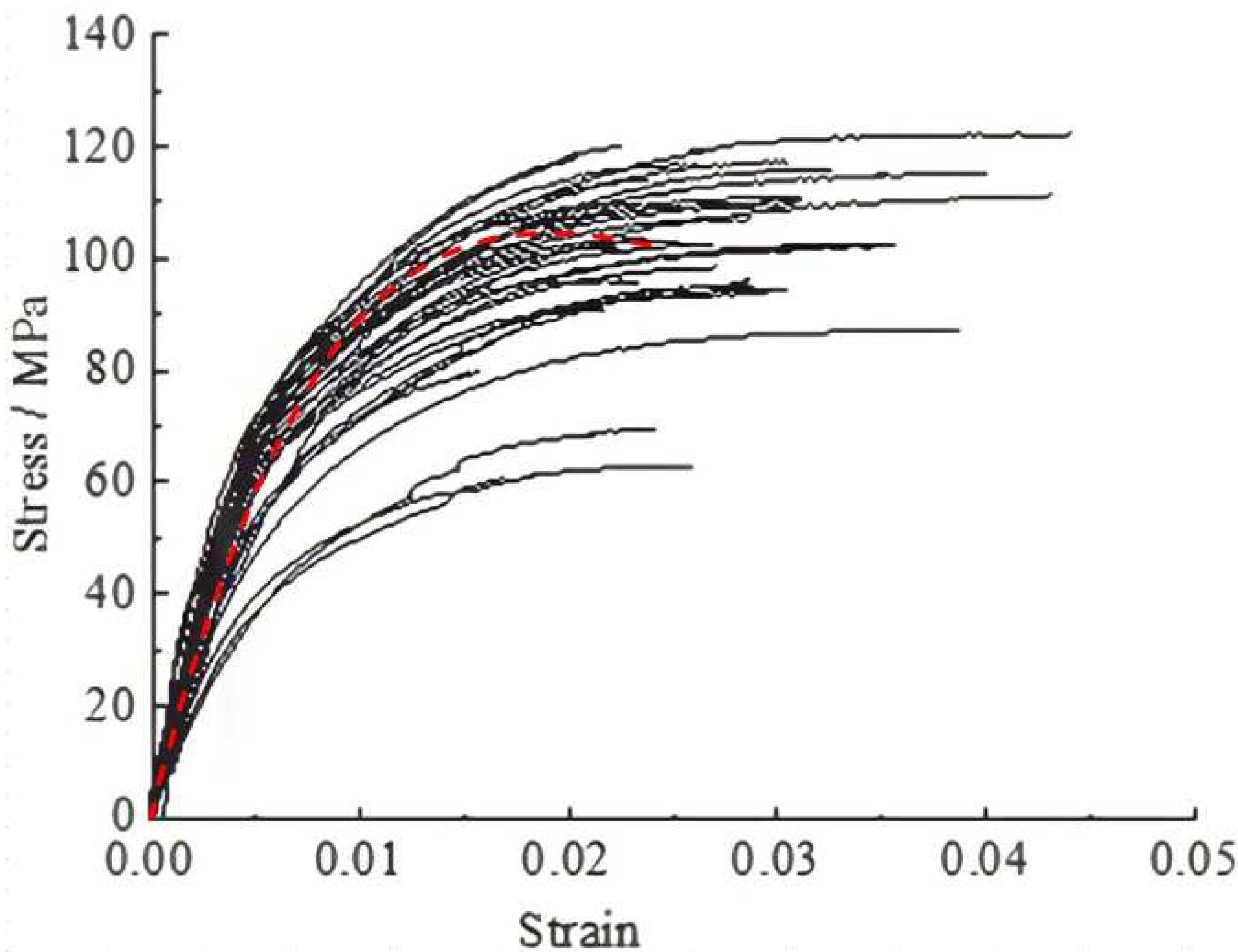


Figure 33: MPM Compression test result (Red dashed lines) compared to experimental result of Phyllostachys edulis bamboo by Li et al. [30]

# 7 DISCUSSION AND CONCLUSION

## 7.1 Material points number Influence

### 7.1.1 Material points number impact on displacement response

In this research, a convergence study was performed to examine the effect of the material point number on the simulated results. In the beginning, the analysis of free vibration of the bar started with the minimum possible number of material points with$10 \times 1$(i.e., 10 here represents the material point number in the x-direction, and 1 reflects the rows number that the 10 points would be added more in the y-direction). The point displacement shows a non-convergence as the simulation time increase. By applying $20 \times 4$ points for bar modeling, the displacement of the particle was almost identical to the exact solution as the simulated time increased, as shown in Figure 5. As a result, the displacement response converged as the material point analysis increased for axially vibration analysis.

In addition, the static analysis for beams shows good converged results as the material points increase. Following the static cantilever beam analysis, the result of $16 \times 2$ appears result closed to elasticity results, especially when the material point is near to the loaded end. The static simply supported beam also experienced converged displacement response for every material point along the beam as the material point number increased from $8 \times 2$, $16 \times 2$ to $16 \times 4$. The displacement of the expected large value (near to mid-span) was tracked as described in Table[5].

### 7.1.2 Material points number impact on frequency response

As this research aims to analyze the frequency using MPM, the frequency responses have been tracked for different numbers of the material points to measure their influence on frequency values. From the observation of frequency results following Fast Forum Transfer (FFT), the material point number does not affect the frequency due to the constant periodic motion of the whole model which is represented by the analyzed particle with a different number of material points. That satisfies the frequency concept of a wave in general. Even with more time-domain samples, the frequencies of MPM were identical for different point numbers.

## 7.2 Time integration of Material Point Method

After getting the semi-discrete equation, the full discrete one is done by applying a time integration. This integration leads to the acceleration at the nodal function; therefore, the nodal acceleration should be satisfied for every step. In addition, in the material point method, the nodal velocity is deleted after every time step due to the grid reset; therefore, the particle velocity must be mapped to the nodes at the starting point of the time loop. Thus, the material point method follows an explicit formulation to solve the fully discrete equation. This formulation requires very small time steps to ensure the stability of the simulation. As a result, considering this concept is critical to producing stable analysis, especially when the large deformation behavior is simulated.

## 7.3 Strain Measures in Material Point Method

Many strain measures can be used in large deformation formulations based on continuum mechanics. In this study, besides the linear strain measures, the Green Lagrangian strain tensor was examined by including the nonlinear terms in the strain increments function. For the nonlinear beam analysis, due to the small contribution of the nonlinear terms to the strain function. The frequency values experienced a small impact when using the Green Lagrangian tensor which led to conclude that using a linear assumption of strain measure would be sufficient even for the large deformation problems. Table [14] explains the frequency of simply supported beam at different $a/r$ values.

Table 14: Frequency values for different strain measures

| a/r | Green Lagrangian strain measure | Linear strain measure |
|---|---|---|
| 0.1 | 0.38845 | 0.38938 |
| 0.2 | 0.38985 | 0.38985 |
| 0.4 | 0.39698 | 0.39698 |
| 0.6 | 0.40521 | 0.40521 |
| 0.8 | 0.41733 | 0.41733 |
| 1.0 | 0.43210 | 0.43210 |
| 1.5 | 0.48344 | 0.48344 |

## 7.4 Euler-Bernoulli beam behavior

A study of Euler Bernoulli beam assumptions has been done in this research. The aim is to validate the behavior of Euler Bernoulli theory using MPM simulation. It is known that, in Euler-Bernoulli assumptions (thin beams theory), the plane cross-section should be plane after the beam deforms. In addition, this deformed plane section is perpendicular to the beam's natural axis. From these concepts, a simply supported beam under a small deformation assumption of free vibration is examined with different lengths $L = 8$ and $L = 16$. The axial displacement of material points at $\frac{L}{4}$ was tracked to validate the simulated assumptions of thin beam theory that was done in this research. Figure 34 shows the first mode shape of vibrated simply supported beam with $L = 8$, the axial displacement of material points at $\frac{L}{4}$ gives the cross-section behavior close to Timoshenko beam theory (thick beam theory) instead of the thin beam theory assumption as given in Figure 35.

As the beam length increase, the beam behavior expresses the Euler Bernoulli beam theory. This expression can be noted with the same problem for $L = 16$ which the axial displacement of material points at $\frac{L}{4}$ tracked and the result is given in Figure 37; therefore, the MPM model can capture the Euler Bernoulli beam theory as the system get thinner which supports the use of this formulation for beam applications.

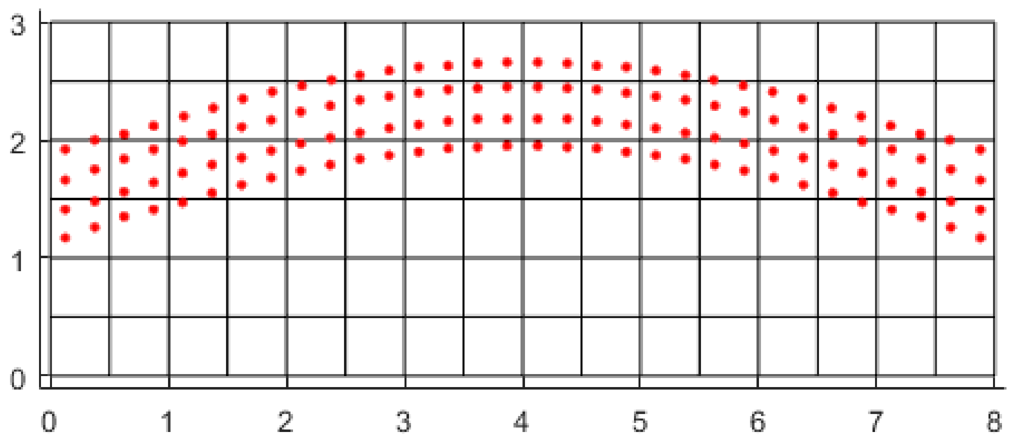


(a) Bending beam

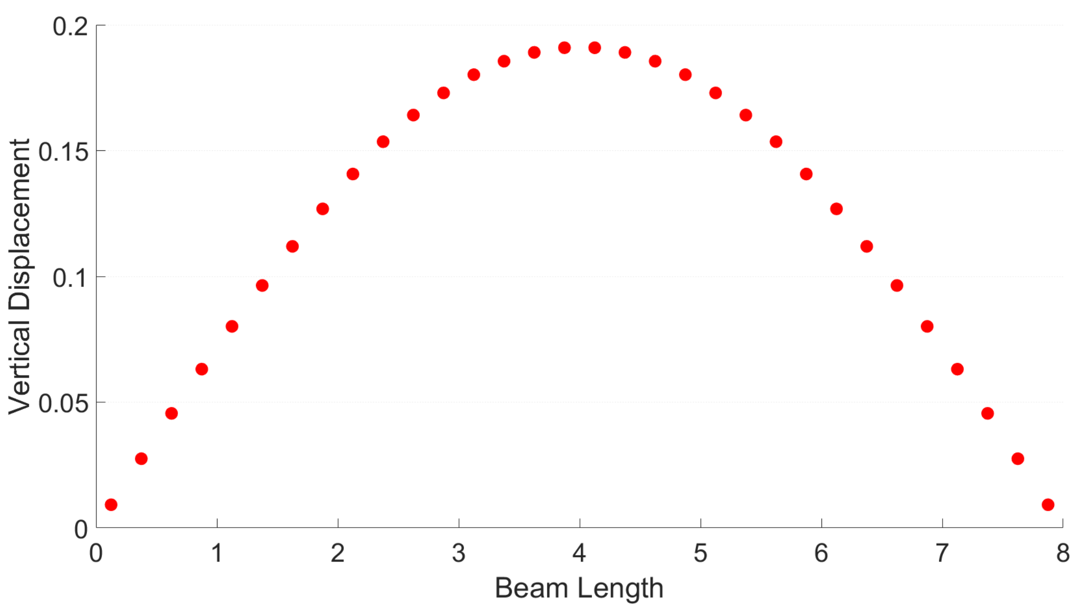


(b) Naturl axis bending

Figure 34: First mode shape of simply supported beam

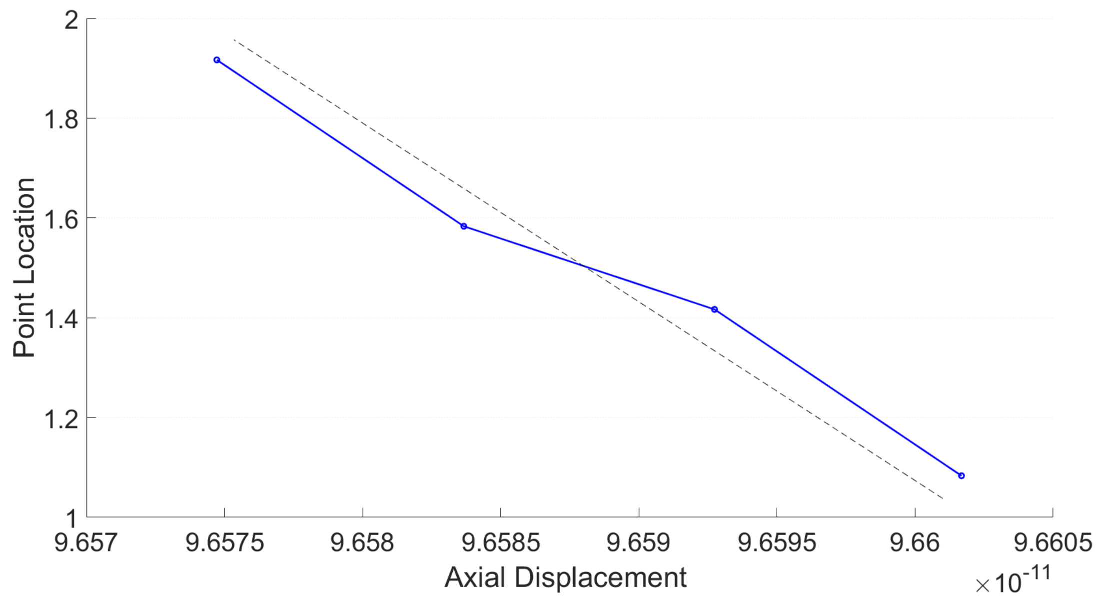


Figure 35: Deformed cross section of beam L = 8 at $\frac{L}{4}$

## 7.5 Element Size Effect

The material point method was tested to get the element size effect on vibrated simply supported beam results for small deformation assumption. The maximum displacement value of the beam was tracked along with different element sizes. The examined elements were taken for the size of $2^{-k}$ where $k$ here applied as [1,2,3,4]. According to Figure 38, as the element size decreases, the error of the maximum displacement decrease and the MPM simulation converges to the exact peak value when the element size is equal to $2^{-4}$.

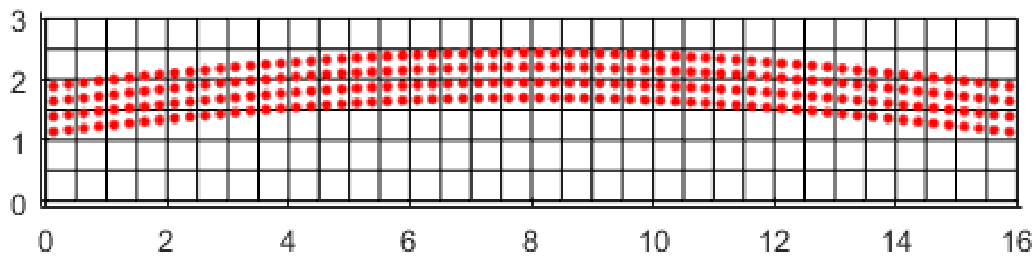


(a) Bending beam

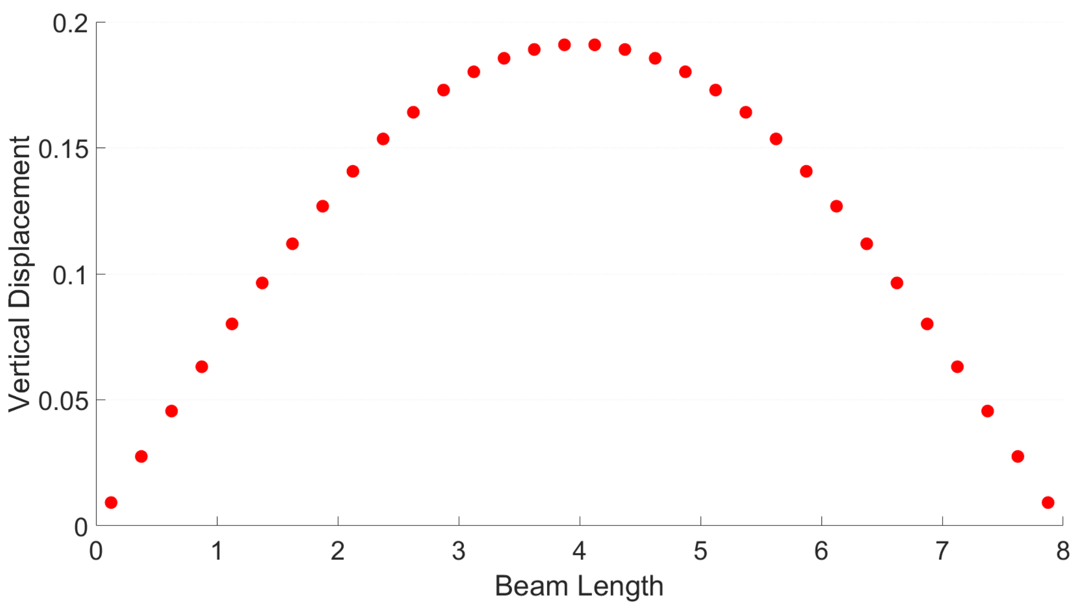


(b) Naturl axis bending

Figure 36: First mode shape of simply supported beam

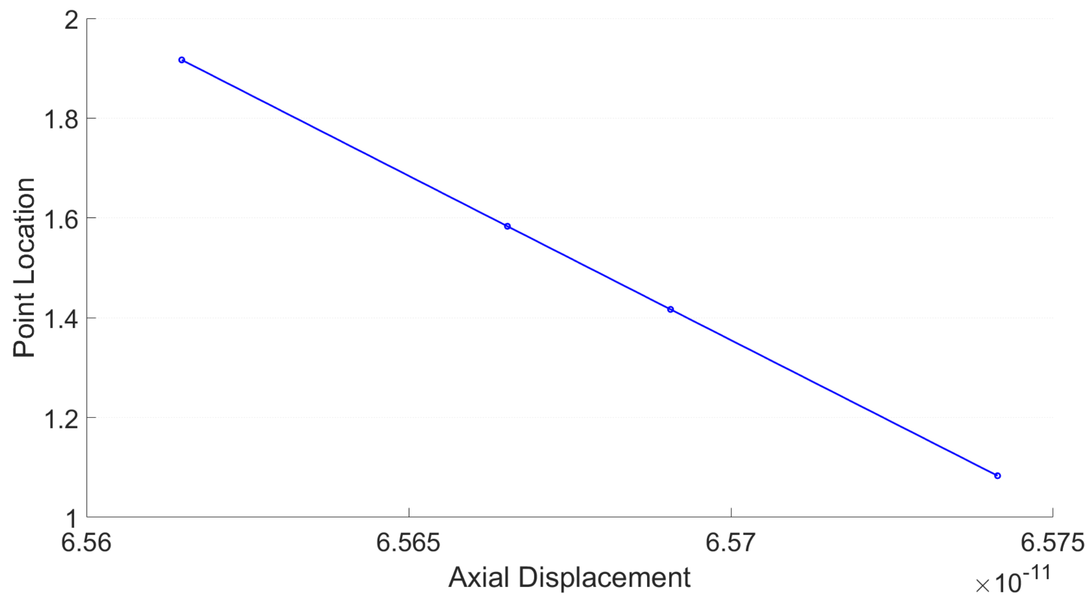


Figure 37: Deformed cross section of beam L = 16 at $\frac{L}{4}$

## 7.6 Conclusion

A geometric and material analysis using the material point method has been done. In this research, the free vibration of beams under the assumptions of small and moderated large deformations is the key analysis that was introduced using MPM. Although the representation of boundary conditions in MPM is more complex than FEM, the simulated responses of beams show satisfactory agreement with exact solutions as well as FEM approximations introduced in this research. The research extended to examine both updated Lagrangian and the total Lagrangian MPM formulations for solid mechanics. In addition, a damage evaluation simulation has been discussed for rock and bamboo type applications and all the related results are verified with experimental findings. The computational algorithms have been implemented using the FORTRAN language through the RMACC Summit Supercomputer platform. The modified updated stress last (MUSL) formulation exhibit considerable and strong results along different assumptions made in this analysis as the very large deformation analysis performed using TLMPM. Generally, MPM behaves appropriately under the external force impact; however, this does not prevent the effects of velocity assumption

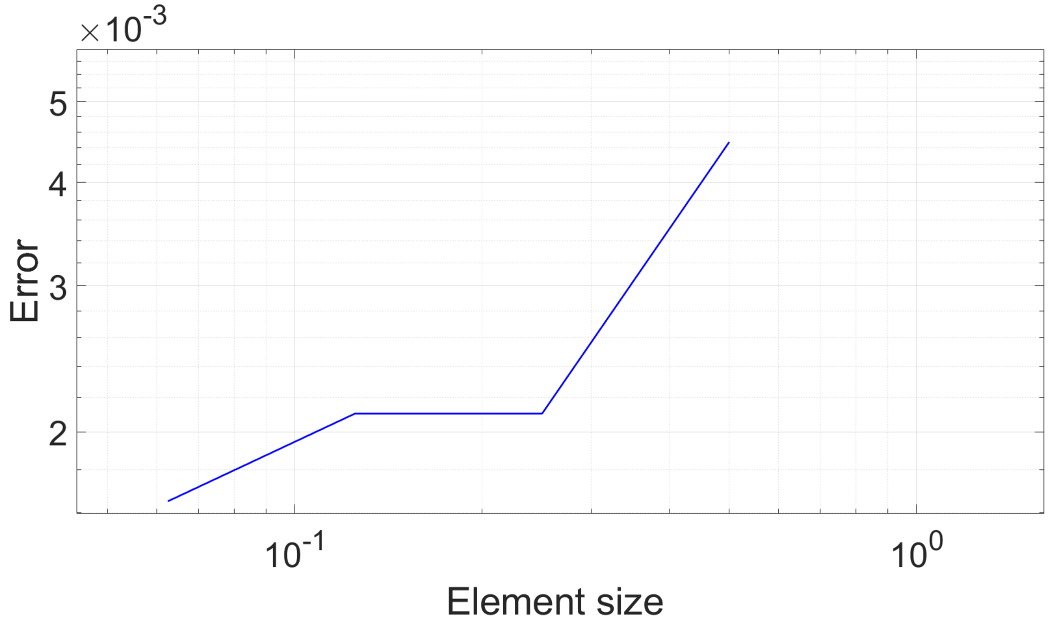


Figure 38: Element size effect of material point method

that collaborate to predict the free vibration behavior in this analysis, which can be noted in the frequency analysis done in two different ways.

MPM has been used for over two decades, creating an efficient algorithm for solid mechanics simulations. Based on the outcomes of this research, MPM can be a reliable formulation of different structural elements like beams and bars. Improvement of frequency analysis is recommended as where it is done for FEM analysis. Also, the MPM should be tested for other beam theories with representations of their assumptions.

# References

[1] M. H. Abedinnasab, H. Zohoor, and Y. J. Yoon. Exact formulations of non-linear planar and spatial Euler-Bernoulli beams with finite strains. *Proceedings of the Institution of Mechanical Engineers, Part C: Journal of Mechanical Engineering Science*, 226(5):1225–1236, 2012.

[2] C. Anastasiadis, I. Stavrakas, D. Triantis, and F. Vallianatos. Correlation of pressure stimulated currents in rocks with the damage parameter. *Annals of Geophysics*, 50(1):1–6, 2007.

[3] S. Andersen and L. Andersen. Material-point method analysis of bending in elastic beams. *Proceedings of the 11th International Conference on Civil, Structural and Environmental Engineering Computing, Civil-Comp 2007*, (7), 2007.

[4] S. G. Bardenhagen. Energy conservation error in the material point method for solid mechanics. *Journal of Computational Physics*, 180(1):383–403, 2002.

[5] K.-J. Bathe. Finite Element Procedures for Solids and Structures - Linear Analysis. (672):1037, 2006.

[6] C.-H. Bauchau, Olivier A and Hong. Large displacement analysis of naturally curved and twisted composite beams. *AIAA journal*, 25(11):1469—-1475, 1987.

[7] L. Beuth, T. Benz, P. A. Vermeer, C. J. Coetzee, P. Bonnier, and P. Van Den Berg. Formulation and validation of a quasi-static Material Point Method. *Proceedings of the 10th International Symposium on Numerical Models in Geomechanics NUMOG 10 - Numerical Models in Geomechanics NUMOG 10*, (April):189–195, 2007.

[8] S. Chucheepsakul, Suraphan Buncharoen, and T. Huang. ELASTICA OF SIMPLE VARIABLE-ARC-LENGTH BEAM SUBJECTED TO END MOMENT. 121(July):767–772, 1995.

[9] A. de Vaucorbeil, V. P. Nguyen, and C. R. Hutchinson. A Total-Lagrangian Material Point Method for solid mechanics problems involving large deformations. *Computer Methods in Applied Mechanics and Engineering*, 360:112783, 2020.

[10] A. De Vaucorbeil, V. P. Nguyen, S. Sinaie, and J. Y. Wu. *Material point method after 25 years: Theory, implementation, and applications*, volume 53. Elsevier Inc., 1 edition, 2020.

[11] J. Deng and D. Gu. On a statistical damage constitutive model for rock materials. *Computers and Geosciences*, 37(2):122–128, 2011.

[12] H. J. Ding, D. J. Huang, and W. Q. Chen. Elasticity solutions for plane anisotropic functionally graded beams. *International Journal of Solids and Structures*, 44(1):176–196, 2007.

[13] H. J. Ding, D. J. Huang, and H. M. Wang. Analytical solution for fixed-end beam subjected to uniform load. *Journal of Zhejiang University: Science*, 6 A(8):779–783, 2005.

[14] E. P. Eer Nisse. Variational Method for Electroelastic Vibration Analysis. *IEEE Transactions on Sonics and Ultrasonics*, 14(4):153–160, 1967.

[15] D. A. EVENSEN. Nonlinear vibrations of beams with various boundary conditions. *AIAA Journal*, 6(2):370–372, 1968.

[16] A. J. Ferreira, R. C. Batra, C. M. Roque, L. F. Qian, and P. A. Martins. Static analysis of functionally graded plates using third-order shear deformation theory and a meshless method. *Composite Structures*, 69(4):449–457, 2005.

[17] J. M. Gere and S. P. Timoshenko. *Mechanics of Materials*. Number no.4. Brooks/Cole Engineering 198, 1984.

[18] R. A. Gingold and J. J. Monaghan. Smoothed particle hydrodynamics theory and application to non-spherical stars. *Monthly Notices of the Royal Astronomical Society*, 181:375–389, 1977.

[19] F. H. Harlow. The particle-in-cell computing method for fluid dynamics. *Methods Comput. Phys*, 3:319–343, 1964.

[20] P. R. Heyliger and A. Asiri. A total Lagrangian elasticity formulation for the nonlinear free vibration of anisotropic beams. *International Journal of Non-Linear Mechanics*, 118(March 2019):103286, 2020.

[21] P. R. Heyliger and A. Jilani. The free vibrations of inhomogeneous elastic cylinders and spheres. *International Journal of Solids and Structures*, 29(22):2689–2708, 1992.

[22] P. R. Heyliger and J. N. Reddy. A higher order beam finite element for bending and vibration problems. *Journal of Sound and Vibration*, 126(2):309–326, 1988.

[23] A. Humer and H. Irschik. Large deformation and stability of an extensible elastica with an unknown length. *International Journal of Solids and Structures*, 48(9):1301–1310, 2011.

[24] M. Şimşek. Fundamental frequency analysis of functionally graded beams by using different higher-order beam theories. *Nuclear Engineering and Design*, 240(4):697–705, 2010.

[25] H. Irschik and J. Gerstmayr. A continuum mechanics based derivation of Reissner's large-displacement finite-strain beam theory: The case of plane deformations of originally straight Bernoulli-Euler beams. *Acta Mechanica*, 206(1-2):1–21, 2009.

[26] J.U. Brackbill and H.M. Ruppel. FLIP: A method for adaptively zoned, particle-in-cell calculations of fluid flows in two dimensions. *Journal of Computational Physics*, 65(2):314–343, 1986.

[27] L. M. Kachanov. *Introduction to continuum damage mechanics*. 1986.

[28] S. G. Lekhnitskii. *Anisotropic plates*. Foreign Technology Div Wright-Patterson Afb, Oh, 1968.

[29] Lemaitre J. and Chaboche J. Aspect Phenomenological Delay Rupture Pare Endommagement. *J. Mech. Appl.*, 2:317–365, 1978.

[30] H. Li, H. Zhang, Z. Qiu, J. Su, D. Wei, R. Lorenzo, C. Yuan, H. Liu, and C. Zhou. Mechanical properties and stress strain relationship models for bamboo scrimber. *Journal of Renewable Materials*, 8(1):13–27, 2020.

[31] T. Liszka and J. Orkisz. The finite difference method at arbitrary irregular grids and its application in applied mechanics. *Computers and Structures*, 11(1-2):83–95, 1980.

[32] L. B. Lucy. A numerical approach to the testing of the fission hypothesis. 82(12):1013–1024, 1977.

[33] H. M. Ma, X. L. Gao, and J. N. Reddy. A microstructure-dependent Timoshenko beam model based on a modified couple stress theory. *Journal of the Mechanics and Physics of Solids*, 56(12):3379–3391, 2008.

[34] Y. Mahmutoglu. Mechanical Behaviour of Cyclically Heated Fine Grained Rock. *Rock Mechanics and Rock Engineering*, 31(3):169–179, 1998.

[35] J. M. Mäkinen. *Total Lagrangian Reissner's geometrically exact beam element without singularities*, volume 70. 2007.

[36] J. Meng, H. Mattsson, J. Laue, and X. Zhang. Large deformation failure analysis of slopes using the smoothed particle finite element method. *IOP Conference Series: Earth and Environmental Science*, 710(1), 2021.

[37] K. K. Minalu. Finite Element Modelling of Skew Slab- Girder Bridges. page 119, 2010.

[38] J. Minguet, Pierre ; Dugundji. Experiments and analysis for composite blades under large deflections. I - Static behavior. *AIAA Journal,*, vol. 28(9):1573–1579.

[39] P. Nanakorn and L. N. Vu. A 2D field-consistent beam element for large displacement analysis using the total Lagrangian formulation. *Finite Elements in Analysis and Design*, 42(14-15):1240–1247, 2006.

[40] B. Nayroles, G. Touzot, and P. Villon. Generalizing the finite element method: Diffuse approximation and diffuse elements. *Computational Mechanics*, 10(5):307–318, 1992.

[41] I. OHNO. Free vibration of a rectangular parallelepiped crystal and its application to determination of elastic constants of orthorhombic crystals. *Journal of Physics of the Earth*, 24(4):355–379, 1976.

[42] M. E. Onyia. a Finite Element Model for the Analysis of Bridge Decks. *Nigerian Journal of Technology*, 27(1):54–60, 2008.

[43] A. Pagani, R. Augello, and E. Carrera. Frequency and mode change in the large deflection and post-buckling of compact and thin-walled beams. *Journal of Sound and Vibration*, 432(January 2020):88–104, 2018.

[44] N. J. Pagano. Exact solutions for composite laminates in cylindrical bending. *Journal of composite materials*, 3(no. 3):398–411, 1969.

[45] P. F. Pai, T. J. Anderson, and E. A. Wheater. Large-deformation tests and total-Lagrangian finite-element analyses of flexible beams. *International Journal of Solids and Structures*, 37(21):2951–2980, 2000.

[46] P. F. Pai, A. H. AU - Nayfeh, and PY. Three-dimensional nonlinear vibrations of composite beams. *Nonlinear Dynamics SP*, 156(Chordwise excitations JO), 1991.

[47] P. F. Pai and A. H. Nayfeh. A fully nonlinear theory of curved and twisted composite rotor blades accounting for warpings and three-dimensional stress effects. *International Journal of Solids and Structures*, 31(9):1309–1340, 1994.

[48] S. K. Park and X. L. Gao. Bernoulli-Euler beam model based on a modified couple stress theory. *Journal of Micromechanics and Microengineering*, 16(11):2355–2359, 2006.

[49] J. N. Reddy. Nonlocal theories for bending, buckling and vibration of beams. *International Journal of Engineering Science*, 45(2-8):288–307, 2007.

[50] E. Reissner. On one-dimensional finite-strain beam theory: The plane problem. *Zeitschrift für angewandte Mathematik und Physik ZAMP*, 23(5):795–804, 1972.

[51] ROLF WESTLUND. Damage Induced. *In. J. Non-Linear Mechanics.*, 14(4):149–161, 1979.

[52] G. Rousselier. FINITE DEFORMATION CONSTITUTIVE RELATIONS INCLUDING DUCTILE FRACTURE DAMAGE Gilles Rousselier To cite this version : HAL Id : hal-02060680. 1981.

[53] B. V. Sankar. An elasticity solution for functionally graded beams. *Composites Science and Technology*, 61(5):689–696, 2001.

[54] B. M. Shahrooz, I. K. Ho, A. E. Aktan, R. de Borst, J. Blaauwendraad, C. van der Veen, R. H. Iding, and R. A. Miller. Nonlinear Finite Element Analysis of Deteriorated RC Slab Bridge. *Journal of Structural Engineering*, 120(2):422–440, 1994.

[55] M. Steffen, R. M. Kirby, and M. Berzins. Decoupling and balancing of space and time errors in the material point method (MPM). *INTERNATIONAL JOURNAL FOR NUMERICAL METHODS IN ENGINEERING*, (February):1102–1119, 2008.

[56] D. J. Steigmann and M. G. Faulkner. Variational theory for spatial rods D.J. STEIGMANN and M.G. pages 1–26, 1993.

[57] D. Sulsky, Z. Chen, and H. L. Schreyer. A particle method for history-dependent materials. *Computer Methods in Applied Mechanics and Engineering*, 118(1-2):179–196, 1994.

[58] D. Sulsky and H. L. Schreyer. Axisymmetric form of the material point method with applications to upsetting and Taylor impact problems. *Computer Methods in Applied Mechanics and Engineering*, 139(1-4):409–429, 1996.

[59] D. Sulsky, S. J. Zhou, and H. L. Schreyer. Application of a particle-in-cell method to solid mechanics. *Computer Physics Communications*, 87(1-2):236–252, 1995.

[60] K. S. Surana. Geometrically non-linear formulation for two dimensional curved beam elements. *Computers and Structures*, 17(1):105–114, 1983.

[61] G. J. N. TIMOSHENKO S. *Theory of Elasticity*. McGraw-Hill Book Company." Inc., New York, 1951.

[62] D. H. Y. W. Weaver Jr., S. P. Timoshenko. *Vibration Problems in Engineering, 5th Edition*. John Wiley and Sons Limited, 1990.

[63] S. Woinowsky-Krieger. The Effect of an Axial Force on the Vibration of Hinged Bars.pdf, 1950.

[64] T. Y. Yang. Matrix displacement solution to elastica problems of beams and frames. *International Journal of Solids and Structures*, 9(7):829–842, 1973.

[65] F. Zhu, J. Zhao, S. Li, Y. Tang, and G. Wang. Dynamically Enriched MPM for Invertible Elasticity. *Computer Graphics Forum*, 36(6):381–392, 2017.